Astronomy & Astrophysics

HARPS radial velocity search for planets in the Scorpius-Centaurus association

A combination with the HARPS and SOPHIE young nearby stars (YNS) surveys[⋆]

A. Grandjean[1], A.-M. Lagrange[2,1,3], N. Meunier[1], G. Chauvin[1], S. Borgniet[2], S. Desidera[4], F. Galland[1], F. Kiefer[2], S. Messina[5], D. Iglesias[12], B. Nicholson[6,7], B. Pantoja[8], P. Rubini[9], E. Sedaghati[10], M. Sterzik[11], and N. Zicher[6]

[1] Univ. Grenoble Alpes, CNRS, IPAG, 414 Rue de la Piscine, 38400 Saint-Martin-d'Hères, France
  e-mail: Antoine.Grandjean1@univ-grenoble-alpes.fr
[2] LESIA, Observatoire de Paris, Université PSL, CNRS, Sorbonne Université, Université de Paris, 5 place Jules Janssen, 92195 Meudon, France
[3] IMCCE – Observatoire de Paris, 77 Avenue Denfert-Rochereau, 75014 Paris, France
[4] INAF – Osservatorio Astronomico di Padova, Vicolo dell'Osservatorio 5, 35122 Padova, Italy
[5] INAF – Osservatorio Astrofisico di Catania, via Santa Sofia, 78 Catania, Italy
[6] Sub-department of Astrophysics, Department of Physics, University of Oxford, Denys Wilkinson Building, Keble Road, Oxford OX1 3RH, UK
[7] University of Southern Queensland, Centre for Astrophysics, WestStreet, Toowoomba, QLD 4350, Australia
[8] Departamento de Astronomía, Universidad de Chile, Camino al Observatorio, Cerro Calán, Santiago, Chile
[9] Pixyl, 5 Avenue du Grand Sablon, 38700 La Tronche, France
[10] European Southern Observatory, Alonso de Córdova 3107, Santiago, Chile
[11] European Southern Observatory, Karl-Schwarzschild-Str 1, 85748 Garching, Germany
[12] School of Physics and Astronomy, Sir William Henry Bragg Building, University of Leeds, Leeds LS2 9JT, UK

ABSTRACT

Context. The Scorpius-Centaurus (Sco-Cen) young and nearby massive star-forming region is particularly well suited for extrasolar planet searches with both direct imaging and radial velocity (RV) techniques. The RV search, however, is challenging, as the stars are faster rotators on average than their older stellar counterparts of similar spectral types. Moreover, the RV time series show strong signatures of stellar variability (spots and faculae) and/or stellar pulsations.
Aims. Our aim is to search for giant planets (GPs) and brown dwarfs at short orbital distances around star members of the Sco-Cen association. We also aim at using these data together with others available on young stars to estimate the GP occurrence rate for young stars for periods of up to 1000 days.
Methods. We used the High Accuracy Radial velocity Planet Searcher (HARPS) spectrograph on the 3.6 m telescope at the La Silla Observatory to monitor 88 $A - F$ Sco-Cen stars. To improve our statistics and analysis, we combined this survey with two previous surveys that focused on young nearby stars (YNS) to compute companion occurrence rates from a sample of 176 young $A - M$ stars.
Results. We report the discovery of a massive hot-Jupiter candidate around HD 145467, together with the discovery of one probable short-period ($P < 10$ days) brown dwarf around HD 149790. In addition, we confirm the binary nature of eight single-line binaries: HD 108857, HD 108904, HD 111102, HD 114319, HD 121176, HD 126488, HD 126838, and HD 133574. From our sample, we obtain a GP ($m_c \in [1; 13]\,M_{Jup}$) occurrence rate of $0.7^{+1.6}_{-0.2}\%$ for periods between 1 and 1000 days and a brown dwarf ($m_c \in [13; 80]\,M_{Jup}$) occurrence rate of $0.6^{+1.4}_{-0.2}\%$, in the same period range. In addition, we report a possible lack of close ($P \in [1; 1000]$ days) GPs around young F-K stars compared to their older counterparts, with a confidence level of 95%.

Key words. techniques: radial velocities – stars: activity – binaries: spectroscopic – planetary systems – starspots – stars: variables: general

1. Introduction

The discovery of the 5000[1] exoplanets and brown dwarf (BD) companions known to date has shown the importance of early stages of planet formation and evolution. This is the case, for instance, for hot Jupiters (HJs), which did not form in situ, and moved in a second step toward the star. While models predict that giant planets (GPs) form beyond a few au (Pollack et al. 1996), disk-planet interactions (Kley & Nelson 2012) or gravitational interactions with a third body may cause significant planet migration (Teyssandier et al. 2019) and may thus explain the HJs that are observed around solar- to late-type main-sequence (MS) stars. Radial velocity (RV) studies of young planets in particular can help constrain the timescales associated with planet migration.

Young stars have been poorly studied with RV techniques, however, because activity or pulsations usually induce high RV variations (jitters), with amplitudes up to a few km s^{-1}

[⋆] Tables A.1–A.6 are only available at the CDS via anonymous ftp to cdsarc.cds.unistra.fr (130.79.128.5) or via https://cdsarc.cds.unistra.fr/viz-bin/cat/J/A+A/669/A12
[1] exoplanet.eu

(Lagrange et al. 2013; Grandjean et al. 2020), which is much higher than the planet-induced signals. Activity has led to several false planet detections in the past (Huélamo et al. 2008; Figueira et al. 2010; Soto et al. 2015). Moreover, young stars are generally faster rotators than their older counterparts (Stauffer et al. 2016; Rebull et al. 2016; Gallet & Bouvier 2015), which leads to broader stellar absorptions, and hence, lower precision on the measured RV.

Previous RV surveys carried out on young stars (<300 Myr) showed no evidence for young HJs (Esposito et al. 2006; Paulson & Yelda 2006; Grandjean et al. 2020, 2021). Detections of young HJs were reported using spectropolarimetric techniques, but the detections are still debated (Carleo et al. 2018; Donati et al. 2020; Damasso et al. 2020). On the other hand, young HJs have been found by transit photometry (Collier Cameron et al. 2010; van Eyken et al. 2012; Deleuil et al. 2012; Mann et al. 2016; Alsubai et al. 2017; David et al. 2019; Rizzuto et al. 2020), and some of them were confirmed with RV methods (Deleuil et al. 2012; Alsubai et al. 2017). Finally, no BDs with periods shorter than 10 days were found with RV around young stars, although one was discovered via transit (Jackman et al. 2019). Therefore, the occurrence rates of young HJs and young short-period BDs still need to be determined with accuracy.

We carried out three RV surveys on young stars from A to M types with the final aim of coupling RV data with direct-imaging data. This will permit exploring the stellar environments from a fraction of au to hundreds of au and then to estimate GP and BD occurrence rates in this semimajor axis (sma) range. The first, southern, survey was performed with the HARPS[2] spectrograph on young nearby stars (YNS); its results are presented in Grandjean et al. (2020). The second, northern, survey was performed with the SOPHIE spectrograph and is reported in Grandjean et al. (2021). The latter paper also presents a statistical analysis that combines the results of the two surveys. Our third survey, also performed with the HARPS instrument, focuses on star members of the Scorpius-Centaurus (Sco-Cen) association. Focusing on a given association ensures a homogeneous sample in age, and allows us to study specific stages in the formation of planetary systems. At an age of 3–18 Myr (Pecaut & Mamajek 2016), Sco-Cen is well suited for studying the early stages of planet formation. It is also of pivotal importance because: Several planets were imaged in the association: HD106906 b (Bailey et al. 2014), HD95086 b (Rameau et al. 2013), UScoCTIO 108 b (Béjar et al. 2009), GSC06214-00210 b (Ireland et al. 2011), 1RXS J160929.1-210524 b (Lafrenière et al. 2008), HD 116434 b (Chauvin et al. 2017b), PDS 70 b and c (Keppler et al. 2018; Haffert et al. 2019), TYC 8998-760-1 b and c (Bohn et al. 2020a,b), and TYC 8984-2245-1 (Bohn et al. 2021), as well as numerous BDs (Hinkley et al. 2015); Moreover, numerous stars of this association present infrared (IR) excesses. In a growing number of cases, disks that caused these excesses have been resolved; they exhibit structures (gaps, rings, and spirals) that might be indicative of the presence of as yet unseen planets (Pecaut & Mamajek 2016; Bonnefoy et al. 2017; Matthews et al. 2017; Keppler et al. 2018; Garufi et al. 2018; Bohn et al. 2019); In addition, its relative proximity (Upper Scorpius: 145 pc; Upper Centaurus-Lupus: 140 pc; Lower Centaurus-Crux: 140 pc; de Zeeuw et al. 1999) permits searching for GPs in direct imaging down to 15–20 au with current instrumentation (Vigan et al. 2021). RV studies nicely complement the searches for planets at shorter separations.

In this paper, we describe this HARPS Sco-Cen survey and present out results. We describe the sample in Sect. 2 and describe the detection of GP, BD, or stellar companions in Sect. 3. We finally combine the HARPS and SOPHIE YNS surveys mentioned above with the present one for a global statistical analysis to derive GP and BD occurrence rates (Sect. 4).

2. Description of the Sco-Cen RV survey

2.1. Sample

Our initial sample included 107 star members of the Sco-Cen association with a distance lower than 150 pc according to their HIPPARCOS[3] parallaxes (van Leeuwen 2007). Most of our targets are also part of the SPHERE[4] GTO[5] SHINE[6] survey sample (Chauvin et al. 2017a; Desidera et al. 2021). We chose to limit our sample below 150 pc to ensure the best detection limits with SPHERE at separations larger than typically 15 au. The *Gaia* mission revised the individual distances of the targets, which now range from 86 to 177 pc (Gaia Collaboration 2020). We then excluded the stars that were identified as binaries with a separation smaller than 2 arcsec to avoid contamination by the second component of the system in the 1 arcsec Mayor et al. (2003) fiber. In addition, five targets[7] were not observed because telescope time was limited.

We measured the projected rotational velocity ($v \sin i$) of the remaining 88 stars[8]. The $v \sin i$ of 19 stars is too high to allow computing the RV ($v \sin i > 300$ km s^{-1}) or computing the bisector ($v \sin i > 150$ km s^{-1})[9]. They were therefore excluded from our analysis. Our final sample (hereafter referred to as the Sco-Cen final sample) accordingly includes 69 targets. This sample has 4 targets in common with the HARPS YNS survey: HD 95086, HD 102458, HD 106906, and HD 131399.

The Sco-Cen final sample (cf. Fig. 1) includes 58 A0-F5 stars ($B - V$ in the range $[-0.05 : 0.52[$) and 11 F6-K5 stars ($B - V$ in the range $[0.52 : 1.33[$). The main characteristics of the targets are summarized in Fig. 1 and Table A.1. Their ages range from 10 to 30 Myr, with a median of 16 Myr (cf. Appendix B for the age determination). The typical uncertainty on the ages is smaller than 8 Myr. This sample is therefore compact in terms of age. The stellar V-band magnitudes range between 5.7 and 12.2, with a median of 8.6, and their masses are between 0.81 and 2.87 $M_\odot$, with a median of 1.5 $M_\odot$ (cf. Appendix B for the mass determination). The stellar $v \sin i$ range from 4 to 110.4 km s^{-1}, with a median of 38.8 km s^{-1}. We note that the median of these projected rotational velocities is higher than that of our previous HARPS YNS (Grandjean et al. 2020) and SOPHIE YNS surveys because most of the stars are of early spectral types and are younger (Stauffer et al. 2016; Rebull et al. 2016; Gallet & Bouvier 2015).

2.2. Observations

The observations of these 69 stars were performed between 2018 and 2020. Some stars were previously observed as part of a

---
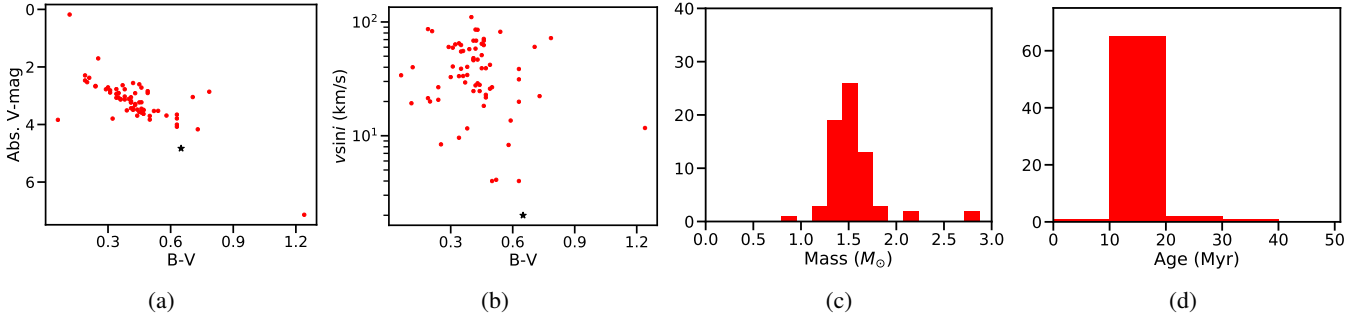
Fig. 1. Main physical properties of our HARPS Sco-Cen sample (red dots). (*a*) Absolute *V*-magnitude vs. *B* − *V*. The solar parameters are displayed (black star) for comparison. (*b*) $v \sin i$ vs. *B* − *V* distribution. (*c*) Mass histogram (in $M_\odot$). (*d*) Age histogram.
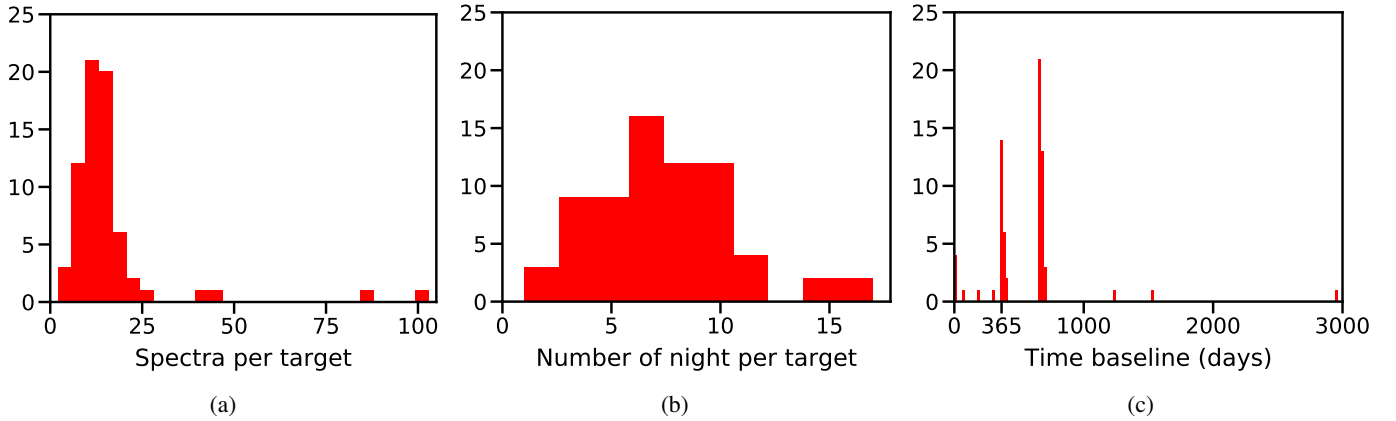
Fig. 2. Observation summary. (*a*) Histogram of the number of spectra per target. (*b*) Histogram of the number of nights per target. (*c*) Histogram of the time baselines.

previous HARPS YNS survey (Grandjean et al. 2020) and as part of previous surveys made by Borgniet et al. (2014, 2017, 2019). The time baselines for these stars is then longer than 2 yr, and in some cases, it is up to 8 yr. The median time baseline is 665 days (mean of 572 days), the median number of spectra per target is 13 (mean of 16), and the median number of nights per target is 7 (mean of 7, Fig. 2). Details can be found in Table A.2.

We adopted the observational strategy presented in Borgniet et al. (2014), which consists of recording two spectra per visit and of observing each target on several consecutive nights. This strategy allows sampling the short-term variations of early-type stars. Because telescope time was limited, we were unable to acquire long sequences (>1.5 h) for early-type stars to sample their pulsations, as was done in Borgniet et al. (2014).

2.3. Observables

We used the software called "spectroscopic data via analysis of the Fourier interspectrum radial velocities" (SAFIR; Galland et al. 2005b) to derive the RVs and, whenever possible, the cross-correlation function (CCF), the bisector velocity span (BVS), the star $v \sin i$ (from the full width at half maximum of the CCF), and the $\log R'_{HK}$ from the HARPS spectra. SAFIR builds a reference spectrum from the median of all spectra available for a given star and computes the RVs relative to the reference spectrum in Fourier space. The efficiency of this method was demonstrated in the search of low-mass companions around AF-type MS stars (Galland et al. 2005a). To select the spectra that were used to build the reference, we used the quality selection criteria that were used for the HARPS YNS survey (Grandjean

et al. 2020): $S/N_{550\,\mathrm{nm}} \in [80; 380]$[10], $sec\ z < 3$ and $\chi^2 < 10$. However, not enough good-quality spectra were available for some stars (HD 100282, HD 106473, HD 109832, HD113524, HD 113556, HD 113901, HD 114082, HD 115361, HD 119511, HD 120326, HD 121189, HD 125912, HD 126488, HD 129590, and HD 137057). For these stars, we adopted a relaxed selection threshold of the signal-to-noise ratio (S/N) at 550 nm down to 30. We verified that the additional spectra did not substantially degrade the quality of the reference spectra. In the case of the faint (*V* ∼ 12.2) PDS 70, we decreased the S/N threshold to 14 (the S/N at 550 nm of the spectra range between 15 and 40).

We did not correct the RVs for the drift induced by the secular acceleration as its amplitude (∼0.003 m s^{-1} yr^{-1}) is negligible with respect to the RV uncertainties for our stars. The main sources of RV variability (magnetic activity, pulsations, or companions) were identified using either the possible correlation between BVS and RV or the shape of their set of bisectors, as was done in Lagrange et al. (2009, 2013) and Borgniet et al. (2017). Briefly, stars with magnetic activity present a correlation between BVS and RV when their $v \sin i$ is high enough and the stellar lines are resolved (Desort et al. 2007). This is the case for our targets, cf. Table A.1. Pulsating stars rather present a (BVS, RV) diagram with an infinite slope (hereafter referred to as vertically spread (BVS, RV) diagram). Companion signals can be identified by bisectors that are parallel to each other, and constant (within noise) BVS values; hence the (BVS, RV) diagram shows a slope of 0 (hereafter referred to as horizontally spread (BVS, RV) diagram).

---

[10] Signal-to-noise ratio per pixel between 554.753 and 555.209 nm, estimated with a sampling of one pixel every 2×10^{-12} m.

3. Detected companions in the HARPS Sco-Cen survey

In addition to HD 106906 and HD 131399, which were already known to be spectroscopic binaries (Lagrange et al. 2016, 2017), 13 stars present evidence of a companion in their RV time series.

When enough data were available, we constrained the orbital elements and the $m_c \sin i$ of the companions (SB1, BD, GP) using *yorbit* (Ségransan et al. 2011).

When long-term trends were observed, we used the toy model of Grandjean et al. (2021) to estimate the minimum mass needed for a companion to produce the observed trend. This minimum mass corresponds to the mass below which a companion cannot explain the observed RV amplitude.

3.1. Binaries without orbital solutions

We present below the single-line spectroscopic binaries (SB1) for which the available RV data are insufficient to perform orbital fitting, as well as the double-line spectroscopic binaries (SB2). Associated figures are shown in Figs. C.1 and C.2.

3.1.1. HD 111102

HD 111102 is an F0III-type star with a 1.5 $M_\odot$ companion imaged at 35 mas (4 au projected separation; Bonavita et al. 2022). We observe an amplitude of $10\,\mathrm{km\,s^{-1}}$ in the HD 111102 RVs (cf. Fig. C.1). The bisectors of HD 111102 are parallel to each other (cf. Fig. C.3a), which indicates that the high-amplitude variations are due to a stellar companion. A correlation between BVS and RV ($R = -0.96$, $p_{\mathrm{value}} < 5 \times 10^{-6}\%$, cf. Fig. C.1), in addition to the $\langle \log R'_{\mathrm{HK}} \rangle$ (-4.222, with a standard deviation of 0.006), indicates that the RVs are also affected by the magnetic activity of the star.

3.1.2. HD 114319

HD 114319 (F0) has a visual companion at a separation of ~2.3″ (~235 au projected separation; Janson et al. 2013; Bonavita et al. 2022). The RV time series of HD 114319 show variations of $1\,\mathrm{km\,s^{-1}}$ over 680 days (1.86 yr) with a curvature, in addition to short-term variations of about $100\,\mathrm{m\,s^{-1}}$ (cf. Fig. C.1). The (BVS, RV) diagram shows that the RV variations are due to a companion plus stellar variability. The imaged companion cannot induce the observed trend given its large separation. HD114319 is thus a triple system.

3.1.3. HD 121176

HD 121176 (F8V) shows RV variations with an amplitude of $1\,\mathrm{km\,s^{-1}}$ over one day (cf. Fig. C.1). The (BVS, RV) diagram is spread horizontally. This indicates that the RV variations are due to a stellar companion.

3.1.4. HD 126488

HD 126488 (F2) shows RV variations with an amplitude of $10\,\mathrm{km\,s^{-1}}$. The shape of the (BVS, VR) diagram ($R = -0.04$, $p_{\mathrm{value}} < 92\%$; cf. Fig. C.1) indicates that these variations are due to a companion.

3.1.5. HD 129590

HD 129590 is a G3V type star with a resolved debris disk (Lieman-Sifry et al. 2016; Matthews et al. 2017) that may consist
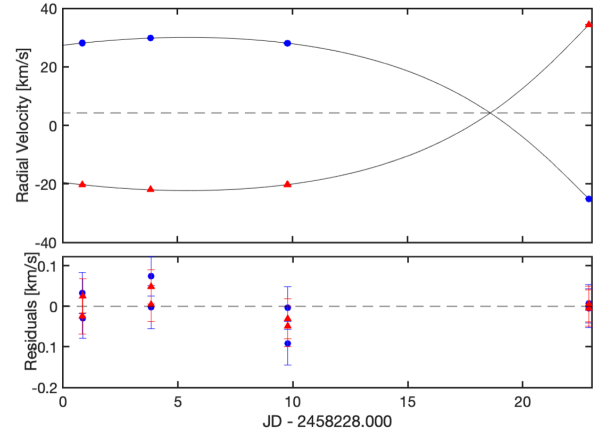
Fig. 3. Keplerian fits of the RV time series of the two components of the HD 137057 AB system, together with the associated residuals.

of two rings (Cotten & Song 2016; Matthews et al. 2018). The variations in CCF (cf. Fig. C.2a), with strong changes over time in the line width, depth, and with a variable width at the continuum, suggest a possible binary of type SB2.

3.1.6. HD 137057

HD 137057 is an F3V type star, known to be the second component of a 120.55″ separation binary system, together with HD 137015 (Andrews et al. 2017). HD 137057 also presents an IR excess (McDonald et al. 2012; Mittal et al. 2015) that is attributed to a debris disk located at 16.6 au.

The CCF shows the double bump that is characteristic of SB2 binary stars (cf. Fig. C.2b). Each peak represents one component of the system. We used TODMOR (Zucker et al. 2003, 2004), which is a 2D CCF technique that can derive the RVs of the two SB2 components at once from our HARPS spectra (thorough details of the methods and practical cases are described in Kiefer et al. 2016, 2018; Halbwachs et al. 2020). The two spectral components were first matched with PHOENIX model spectra around the CaI lines (6120 Å) at four different epochs with the largest CCF-peak separation, leading to $\mathrm{Teff_A} = 6700\,\mathrm{K}$, $\log g_A = 4.4\,\mathrm{cgs}$, $V \sin i_A = 23\,\mathrm{km\,s^{-1}}$, $\mathrm{Teff_B} = 6600\,\mathrm{K}$, $\log g_B = 4.4\,\mathrm{cgs}$, $V \sin i_B = 20\,\mathrm{km\,s^{-1}}$, $[\mathrm{Fe/H}] = -0.3\,\mathrm{dex}$, and a flux ratio in the optical of $F_B/F_A \sim 0.85 \pm 0.05$, with typical uncertainties on $\sigma_{\mathrm{Teff}} \sim 200\,\mathrm{K}$, $\sigma_{\log g} \sim 0.1\,\mathrm{cgs}$, $\sigma_{\mathrm{Fe/H}} \sim 0.1\,\mathrm{dex}$, and $\sigma_{v \sin i} \sim 1\,\mathrm{km\,s^{-1}}$ (Kiefer et al. 2016, 2018). Then these templates were used to calculate a multi-order 2D cross-correlation with the observed spectra using TODMOR. This led to a time series of RVs for each component. Keplerians were simultaneously fit on these RVs, and the common orbital period, time of periastron passage, periastron angle, eccentricity, systemic velocity, and two different RV semi-amplitudes, one for each component (cf. Fig. 3) were varied. From this fit, we estimate a period of $48 \pm 13\,\mathrm{days}$ and a mass ratio of 0.975 ± 0.001 for the HD 137057 AB system. The HD 137015-137057 AB is consequently a triple hierarchical system.

3.1.7. HD 143811

HD 143811 is an F5V type star, presenting an IR excess (Chen et al. 2011; Gáspár et al. 2016) that is attributed to a debris disk located at 8.5 au (Cotten & Song 2016). The CCF shows a double component (cf. Fig. C.2) that might be indicative of an SB2 type binary.
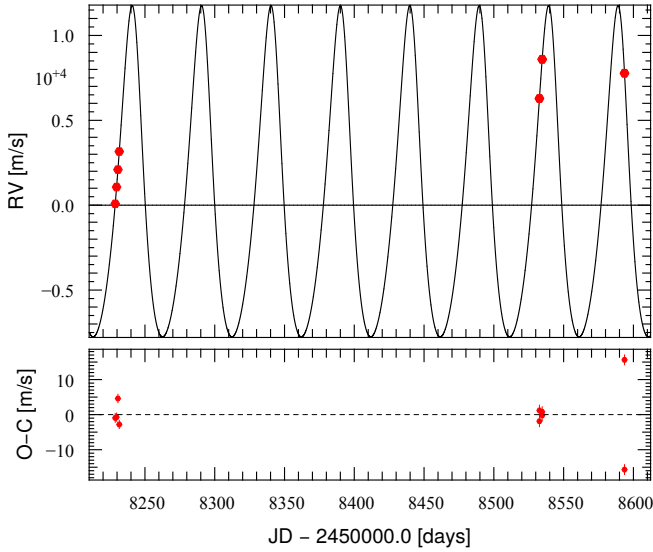
Fig. 4. HD 108857 Keplerian fit and associated residuals.

3.2. Single-line binaries with orbital solutions or constraints, and targets with RV long-term trends

We present hereafter the SB1 binaries for which we were able to constrain the companion properties (cf. Fig. C.4). We also present the stars with a long-term trend for which a linear regression was performed (cf. Fig. C.5).

3.2.1. HD 108857

HD 108857 is an F7V type star with a mass of $1.4\,M_\odot$ (Mittal et al. 2015). It shows an IR excess (Chen et al. 2011; McDonald et al. 2012) that is attributed to two debris belts located at 2.6 and 5.3 au. Direct-imaging observations did not reveal companions (Mamajek et al. 1999; Janson et al. 2013; Nielsen et al. 2019). Finally, HD 108857 presents a proper motion anomaly that can be attributed to a companion (Kervella et al. 2019). The RV time series of HD 108857 presents variations with an amplitude of $10\,\mathrm{km\,s^{-1}}$ that we attribute to a companion. We used *yorbit* to fit the RVs with one Keplerian model to constrain the companion parameters (cf. Fig. 4). The solution of the fit is not unique because only a few spectra were available and the phase coverage is poor. The less eccentric solution we obtained has a period of 49.735 ± 0.007 days, an eccentricity of 0.23 ± 0.02, and an $m_c \sin i$ of $0.21 \pm 0.02\,M_\odot$ ($215 \pm 21\,M_{\mathrm{Jup}}$).

3.2.2. HD 108904

HD 108904 is an F6V type star with a mass of $1.5\,M_\odot$ (Mittal et al. 2015), known to present an IR excess (McDonald et al. 2012). Bonavita et al. (2022) imaged a companion at 54 mas (∼6 au projected separation) with SPHERE and estimated its mass from evolutionary models at $0.18 \pm 0.02\,M_\odot$ ($190^{+20}_{-20}\,M_{\mathrm{Jup}}$). HD 108904 also presents a proper motion anomaly (Kervella et al. 2019) that may have been induced by the imaged companion. We observe RV variations of $4\,\mathrm{km\,s^{-1}}$ over 666 days with a curvature, in addition to a $100\,\mathrm{m\,s^{-1}}$ short-term jitter (cf. Fig. C.4). The (BVS, RV) diagram is spread horizontally ($R = -0.19$, $p_{\mathrm{value}} < 40\%$, cf. Fig. C.4), which indicates that the long-term signal is due to a companion. A Keplerian fit of the RVs alone with *yorbit* (cf. Fig. 5) gives a period of 900 ± 220 days ($2.1^{+0.3}_{-0.4}$ au; 19 ± 3 mas), an eccentricity of 0.76 ± 0.11, and a

mass of $0.24^{+0.07}_{-0.08}M_\odot$ ($247^{+75}_{-86}\,M_{\mathrm{Jup}}$). The sma we found is inconsistent with the projected separation of the imaged companion. This is expected because our RV data do not properly sample the companion orbit. Clearly, more RV and more imaging data are needed to sample the companion orbit properly.

We then used a Markov chain Monte Carlo (MCMC), described in Lagrange et al. (2020), to fit the RVs and the available relative astrometry (Bonavita et al. 2022) of the imaged companion simultaneously. A correct fit of the RVs is obtained with an sma of about 4 au ($P \sim 2400$ days), a high eccentricity (>0.4), and a mass compatible with that deduced from evolution models: ∼$0.2\,M_\odot$ (cf. Figs. 6 and C.6). We stress that the data are sparse, so that these results should be regarded as indicative.

3.2.3. HD 126838

HD 126838 is a $1.78\,M_\odot$ F3V star that is known to present an IR excess (McDonald et al. 2012). It is also known as a visual binary, with a projected separation of 2.93 arcsec (∼354 au projected separation; Mason et al. 2001; Chen et al. 2011; Kervella et al. 2019; Bonavita et al. 2022). Our RVs show a trend with a slope of $7.1\,\mathrm{km\,s^{-1}\,yr^{-1}}$ observed on 398 days. The amplitude of the observed trend is too high to be attributed to a possible magnetic cycle. Short-term variations are present in addition to the trend, with an amplitude of $100\,\mathrm{m\,s^{-1}}$ (cf. Fig. C.5). Moreover, the (BVS, VR) diagram is spread horizontally ($R = 0.29$, $p_{\mathrm{value}} < 48\%$; cf. Fig. C.5) and the bisectors are parallel to each other. The imaged companion cannot induce the observed trend due to its large separation. We therefore attribute the long-term drift to an additional companion, with a minimum mass of $0.25\,M_\odot$ ($260\,M_{\mathrm{Jup}}$), and a period longer than one year. The residuals of a linear regression on the RVs present a standard deviation of $110\,\mathrm{m\,s^{-1}}$, and they are not significantly correlated with BVS ($R = -0.29$, $p_{\mathrm{value}} < 26\%$; cf. Fig. C.5).

The system was identified as a TESS object of interest (TOI 1946). The transiting candidate has a period of 10.845 days and a radius of $30.4 \pm 0.9\,R_\oplus$*** (Bonavita et al. 2022). Bonavita et al. (2022) discussed the probable system architecture, arguing that the companion that causes the transit signature is a star and orbits HD 126838 B. If confirmed, this would make the system a hierarchical quadruple system.

3.2.4. HD 133574

HD 133574 is a $1.6\,M_\odot$ (Pecaut et al. 2012) A9-type star, located at 156.3013 ± 1.7125 pc (Gaia Collaboration 2018), which presents an IR excess (McDonald et al. 2012). Bonavita et al. (2022) imaged a low-mass star companion at 88.9 mas (13.9 au projected separation) and estimated its mass from evolutionary models to be $0.59\,M_\odot$ ($620\,M_{\mathrm{Jup}}$). HD 133574 also presents a proper motion anomaly (Kervella et al. 2019) that might be induced by the imaged companion. We observe a drift in HD 133574 RVs with a slope of $320\,\mathrm{m\,s^{-1}\,yr^{-1}}$ over 681 days. In addition, the RVs present short-term variations with an amplitude of ∼$50\,\mathrm{m\,s^{-1}}$ (cf. Fig. C.5), but these variations are poorly sampled. The HD 133574 bisectors are parallel to each other, and its BVS are not significantly correlated with the RVs ($R = -0.36$, $p_{\mathrm{value}} < 12\%$). This indicates that the trend is due to a companion. Assuming a semimajor axis of 13.9 au, the imaged companion would induce an RV trend with a mean slope of ∼$360\,\mathrm{m\,s^{-1}\,yr^{-1}}$. We therefore attribute the RV trend to this companion.
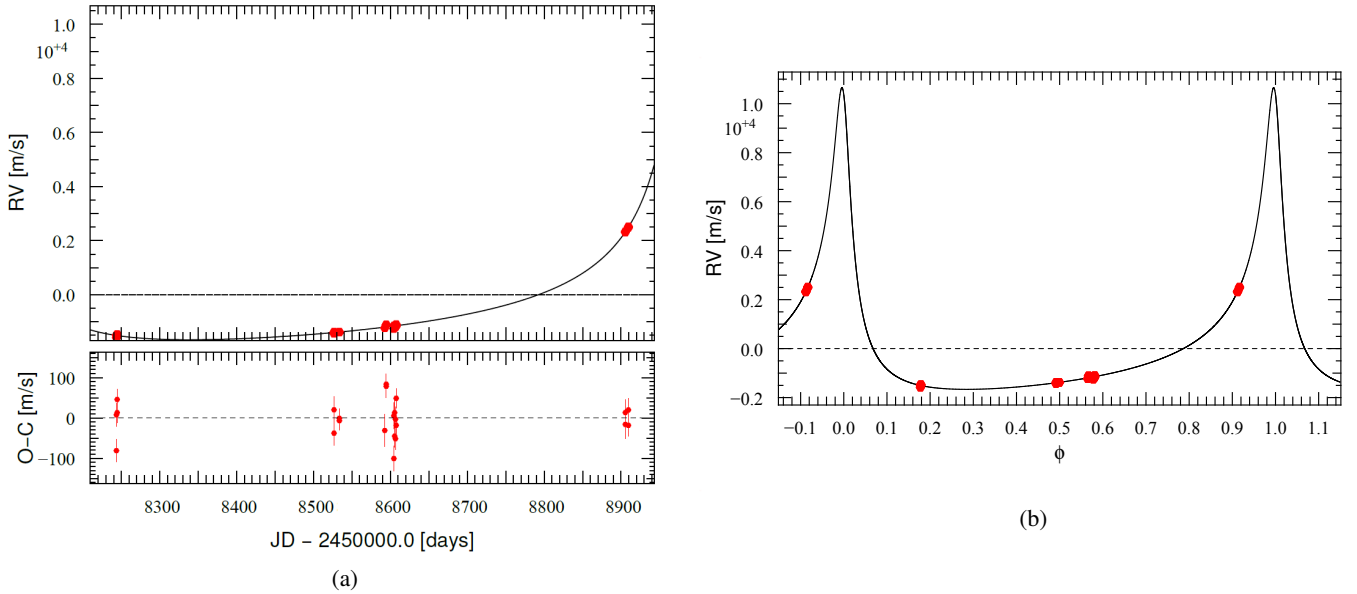
Fig. 5. HD 108904 companion anlysis. (*a*) Best fit of HD 108904's RV with one Keplerian and its associated residuals. (*b*) Phase-folded plot of the fit.
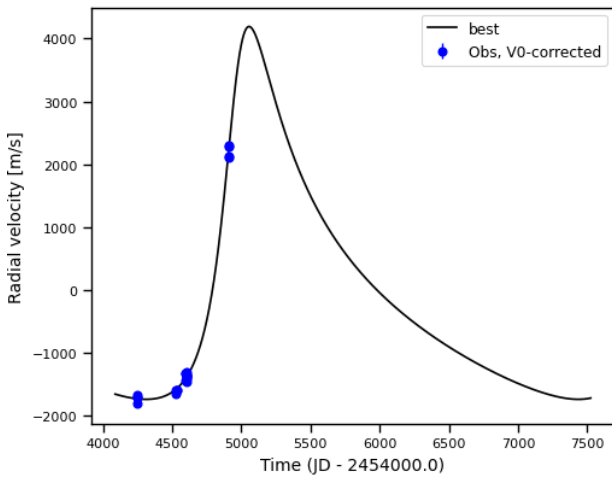
Fig. 6. HD 108904 best fit of the MCMC applied on RV and relative astrometry simultaneously.

3.3. Interesting substellar companions

3.3.1. Probable BD around HD 149790

HD 149790 is an F3V-type star with a mass of 1.4 $M_\odot$ (Pecaut et al. 2012). It shows an IR excess (McDonald et al. 2012), attributed to a debris disk located at 1.2 au (Cotten & Song 2016). Our RV data show variations with amplitude of about 7 km s^{-1} (cf. Fig. 7). The bisectors are roughly parallel to each other (cf. Fig. C.3b) and are spread horizontally (BVS vs. VR diagram: $R = 0.55$, $p_{\text{value}} < 7\%$ cf. Fig. C.4), which indicates the presence of a companion.

The periodogram of the RVs presents peaks above the 1% false-alarm probability (FAP) at 2.26 and 2.35 days, as well as at 6, 6.67, 7.5, and 8.5 days (cf. Fig. 8a). The BVS periodogram does not show peaks above the 10% FAP (cf. Fig. 8b).

To constrain the period and the minimum mass of the companion candidate, we fit the RVs with a Keplerian model (cf. Figs. 9 and 8c) using *yorbit*. We obtain a period of 6.673 ± 0.003 days, a low eccentricity ($e = 0.005 \pm 0.006$), and a $m_c \sin i$

of 42 ± 0.3 M_{Jup}. This companion candidate would therefore be a BD. Additional RV observations are mandatory to definitely confirm the orbital parameters and the $m_c \sin i$ of this companion. If confirmed, it will be the first young (<100 Myr) short-period (<10 days) BD (sin *i*-wise) ever detected with the RV technique, and the second of its kind ever detected, together with NGTS-7A b (Jackman et al. 2019).

The residuals of the fit have an amplitude of 50 m s^{-1}, and the (BVS, RV residuals) diagram is spread vertically (cf. Fig. C.4), which indicates that the variations of the residuals can be due to pulsations. This would explain why the (BVS, VR) diagram of HD 149790 is not completely flat, as it is in fact the combination of a vertically spread diagram due to pulsations and a horizontally spread diagram due to the companion.

3.3.2. GP candidate: HD 145467 b

HD 145467 is a 1.56 $M_\odot$ F0V-type star. We obtained 24 spectra between April 2018 and March 2020 on this star. However, 8 spectra (from the nights of March 12 and 13, 2020) were taken with a lunar angular separation below 9°. To avoid any contamination from the moon, we excluded these spectra from our analysis. The RV variations present a total amplitude of 2.5 km s^{-1}, and the (BVS, VR) diagram is spread both vertically (over 1 km s^{-1}) and horizontally (over 2 km s^{-1}; $R = -0.16$, $p_{\text{value}} < 58\%$, cf. Fig. 10a). This indicates that the RV variations are mainly due to a companion that produces the horizontal spreading, and to stellar pulsations, which produce the vertical spreading. A sequence of six continuous spectra obtained on the night of March 12, 2020, shows RV variations of more than 100 m s^{-1} over 3 h (cf. Fig. 10), associated with BVS variations over 1 km s^{-1}. The (BVS, VR) diagram of this sequence is spread vertically (cf. Fig. 10b), which confirms that the short-term variations are due to pulsations. The RV variations of HD 145467 are then the sum of a companion signal with an amplitude of about 2 km s^{-1} and of pulsations with an amplitude of about 100 m s^{-1}.

We used *yorbit* to constrain the period and $m_c \sin i$ of the companion. The number of data points is small, however, and the data are clearly impacted by pulsations. For simplicity, we therefore assume an eccentricity lower than 0.2. We obtain a period
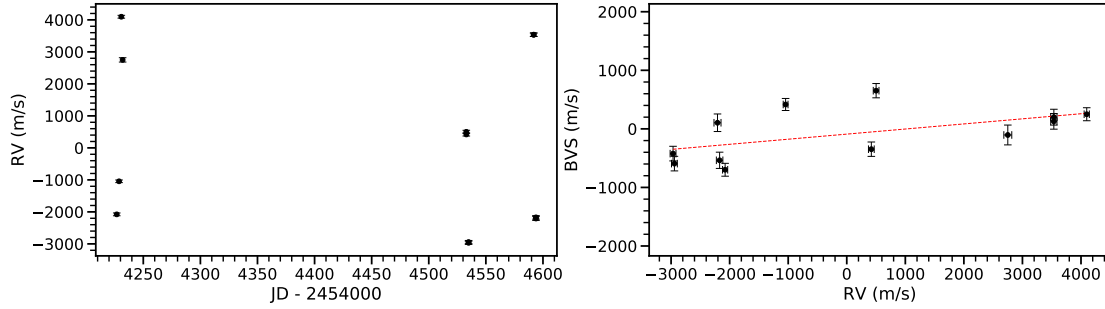
Fig. 7. HD 149790 data. *Left:* RV time variations. *Right:* BVS vs. RV diagram (black) and its best linear model (dashed red line).
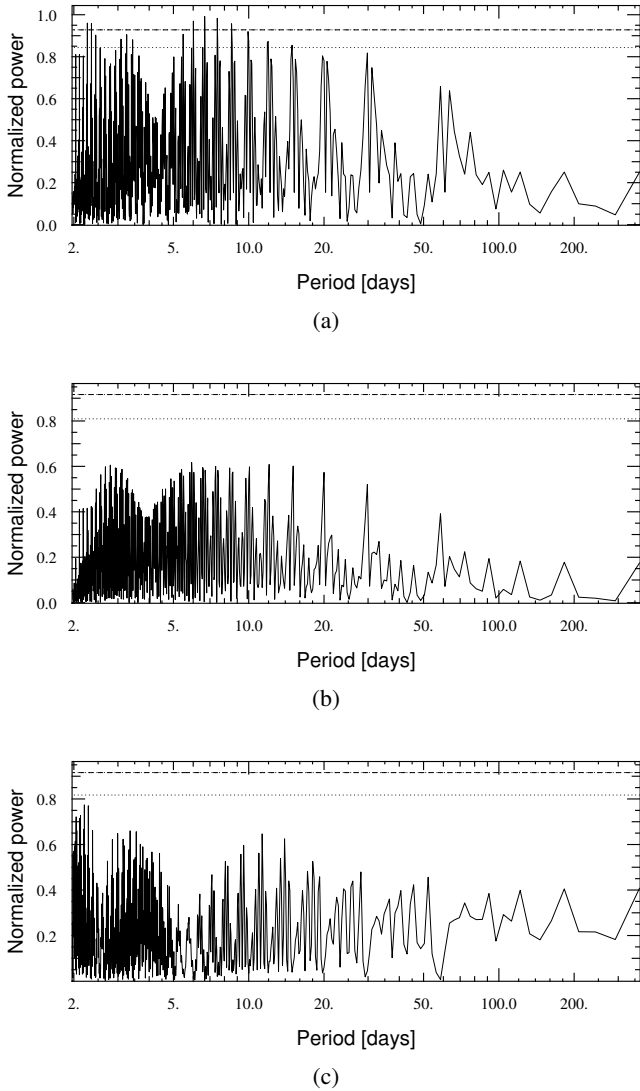
Fig. 8. HD 149790 anylysis. (*a*) Periodogram of the RV time series. (*b*) Periodogram of the BVS time series. (*c*) Periodogram of the residuals after subtracting the best Keplerian fit. The 1% and 10% FAP are presented as dashed and dotted lines, respectively.

of ~5.4 days, and the $m_c \sin i$ is ~13 M_{Jup} (cf. Figs. 11a and 11b). The residuals of the fit present variations with a standard deviation of 70 m s^{-1}, and their (BVS, RV residuals) diagram is spread vertically (cf. Fig. 12). This indicates that the residuals are due to pulsations.

We conclude that HD 145467 has a companion with a minimum mass of ~13 M_{Jup}. However, due to a lack of RV data, its period and eccentricity are not precisely constrained. Additional data are then needed to confirm this HJ or short-period BD companion candidate. If confirmed, this companion would be of particular interest, as only a few confirmed HJs of that age (<20 Myr) are known to date (Collier Cameron et al. 2010; Deleuil et al. 2012; van Eyken et al. 2012; Mann et al. 2016; Alsubai et al. 2017; David et al. 2019; Rizzuto et al. 2020).

3.4. Summary of the detected companions

Eleven spectroscopic binaries (eight SB1 and three SB2) were identified in our analysis of the Sco-Cen final sample; two additional were known. This sample therefore includes 13 spectroscopic binaries (ten SB1 and three SB2). In addition, one short-period ($P < 10$ days) BD companion candidate was identified around HD 149790, and one tentative short-period ($P < 10$ days) companion candidate, at the limit between BD and planets, was identified around HD 145467.

## 4. HARPS Sco-Cen, SOPHIE YNS, and HARPS YNS combined survey analysis

To improve the statistics of GPs around young stars, we combine below the HARPS Sco-Cen survey described above with the SOPHIE (Grandjean et al. 2021) and the HARPS (Grandjean et al. 2020) YNS surveys.

4.1. Combined sample

The HARPS and SOPHIE YNS combined sample included 143 targets (Grandjean et al. 2021). Four of them are in common with our Sco-Cen sample: HD 95086, HD 102458, HD 106906, and HD 131399 (which are part of the HARPS YNS survey).

We excluded the targets whose data were not suitable for the statistical analysis. From the HARPS and SOPHIE YNS combined sample, we excluded the targets that were excluded in Sects. 2.1 and 4.1 of Grandjean et al. (2021): stars whose $v \sin i$ is too high (>300 km s^{-1}) to allow RV measurements, stars that are too old, and binary stars for which the companion signal could not be fitted. From the Sco-Cen survey, we excluded the stars excluded in Sect. 2.1 of this paper. In addition, we excluded the stars with companions whose RV signal could not be fitted: HD 111102, HD 121176, HD 126488, HD 129590, HD 137057, and HD 143811. Finally, we excluded HD 114319 and HD 145467 because their companions still need confirmation.

The final combined sample gathers 176 A0V to M5V targets (cf. Fig. 13) that are suitable for our statistical analysis. Eighty targets have a spectral type between A0 and F5V (B-V $\in [-0.05 : 0.52[$; hereafter AF subsample), 87 have a spectral
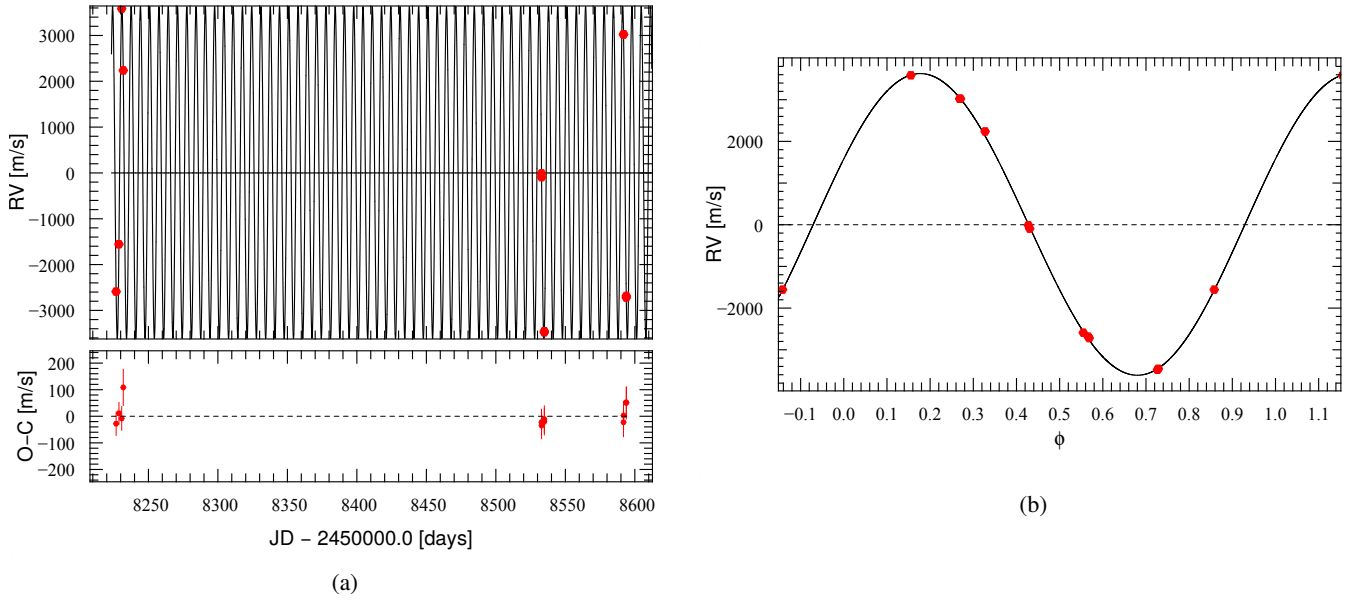
Fig. 9. HD 149790 companion analysis. (*a*) HD 149790 best Keplerian fit (one planet) and its residuals. (*b*) Phase-folded plot of the fit.
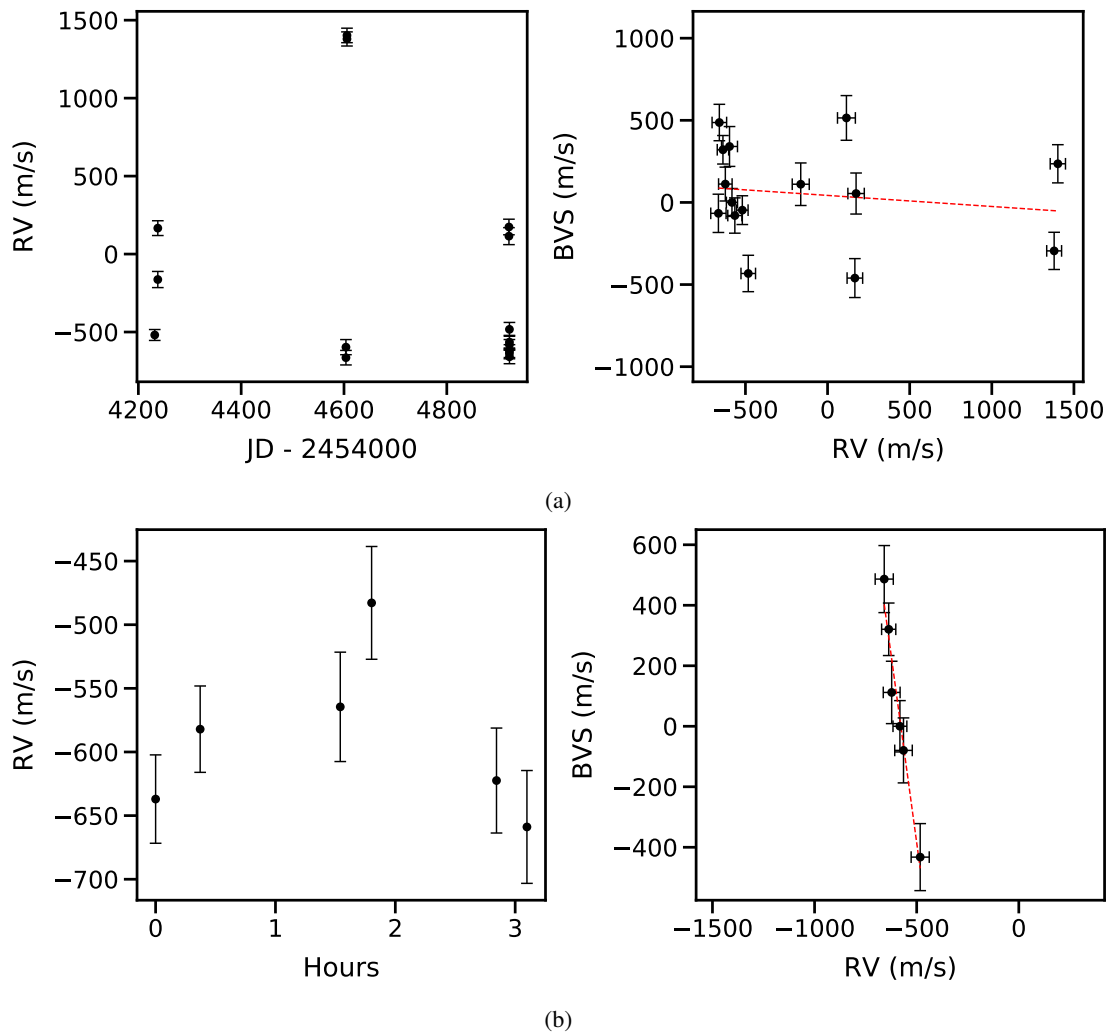
Fig. 10. HD 145467 analysis. (*a*) RV variations (*left*) and corresponding (BVS, VR) diagram (*right*). (*b*) Zoom on a 3-h sequence (*left*) and corresponding (BVS, VR) diagram (*right*).

(a)

(b)
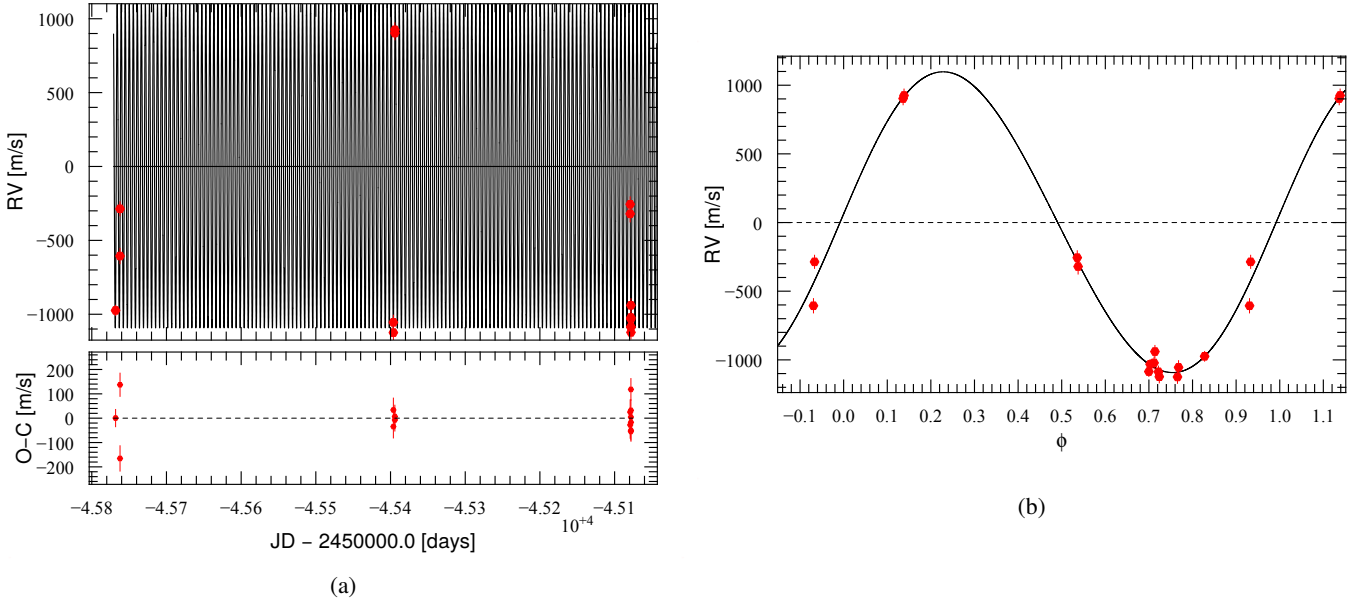
Fig. 11. HD 145467 companion analysis. (*a*) Best one-planet Keplerian fit of HD 145457's RV with $e < 0.2$ and its associated residuals. (*b*) Phase-folded plot of the fit.
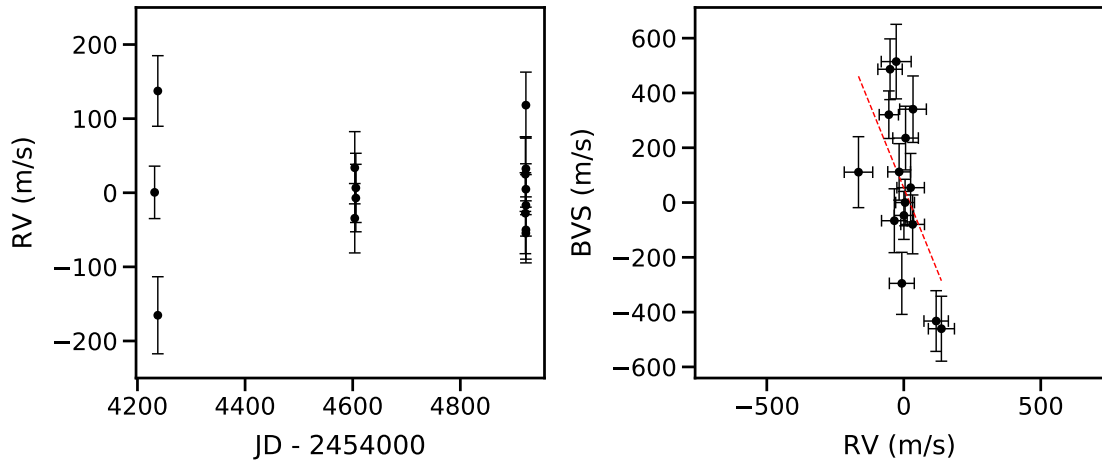
Fig. 12. HD 145467 companion analysis. *Left:* RV residuals of HD 145467 best one-planet Keplerian fit with $e < 0.2$. *Right:* (BVS, RV residuals) diagram and its best linear model (dashed red line).
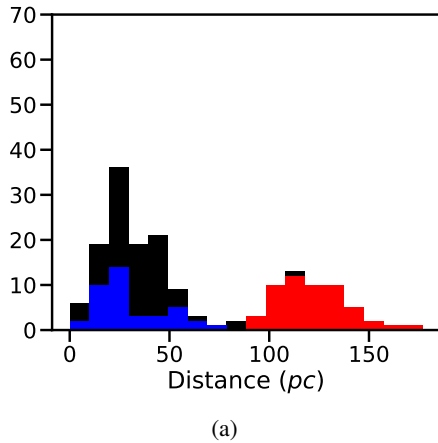
type between F6 and K5 ($B - V \in [0.52 : 1.33[$;hereafter FK subsample), and 9 have a spectral type between K6 and M5 ($B - V \geq 1.33$; hereafter M subsample); Their distances range between 3 and 177 pc, with a median of 43 pc (cf. Fig. 14, Gaia Collaboration 2018). Their projected rotational velocities ($v \sin i$) range from 1.7 to 120 km s^{-1}, with a median of 13.5 km s^{-1}; Their V-band relative magnitude ranges between 1.16 and 12.18, with a median of 8.11; Their masses range between 0.42 and 2.8 $M_\odot$, with a median of 1.2 $M_\odot$ (cf. Fig. 15; cf. Appendix B for the determination of the masses). The AF (FK and M) subsample has a median mass of 1.5 (0.98 and 0.6) solar mass, with a standard deviation of 0.31 (0.22, and 0.08) solar mass; Their median age (cf. histogram in Fig. 15) is 45 Myr (cf. Appendix B for the determination of the ages). Ninety-seven percent are younger than 600 Myr; Their metallicities are close to the solar metallicity (cf. Fig. 16), with a median of 0.0 dex (mean of 0.01 dex) and a standard deviation of 0.18 dex (metallicity measurements are only available for 127 of our targets

in the Strasbourg astronomical data center (hereafter CDS database)); Similarly to the HARPS and SOPHIE YNS surveys (Grandjean et al. 2021), we observe no statistically significant correlation between the metallicity and the $B - V$, nor between the metallicity and the stellar mass in our final combined sample; One hundred and sixty-six stars out of 176 present Ca II emission in their spectra. Figure 17 shows the $\langle \log R'_{HK} \rangle$ vs. $B - V$. The median $\langle \log R'_{HK} \rangle$ is -4.4, with a standard deviation of 0.3. Eight targets present signs of low activity ($\langle \log R'_{HK} \rangle <$ -4.75), 132 are active ($-4.75 < \langle \log R'_{HK} \rangle < -4.2$), and 26 present signs of high activity ($\langle \log R'_{HK} \rangle > -4.2$); Finally, the median time baseline is 906 days (mean time baseline of 1546 days), and the median number of spectra per target is 19 (mean of 67), spaced on a median number of 11 nights (mean of 14, Fig. 18).

Details can be found in the Tables A.1–A.6 (Tables A.3–A.6 are updated versions of the Tables A.1–A.4 presented in Grandjean et al. 2021, respectively).
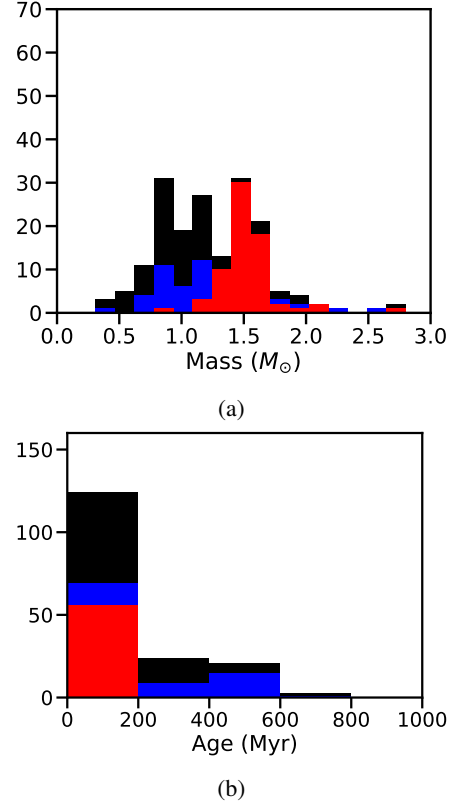
(a)

(b)
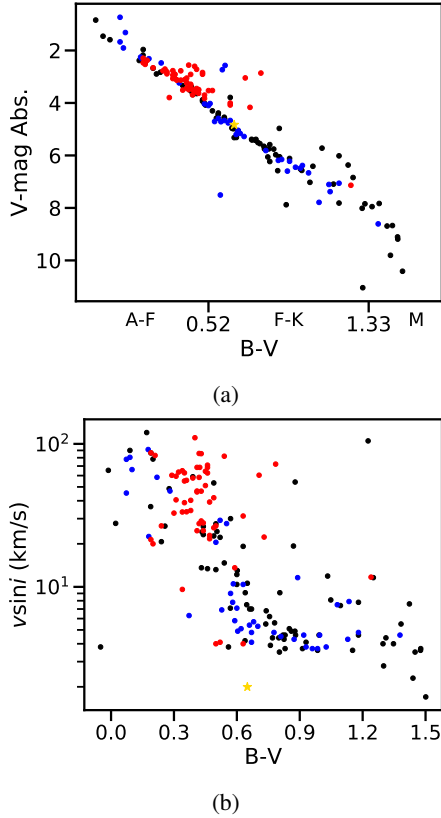
Fig. 13. Main physical properties of our final combined sample. Black shows HARPS YNS targets, blue shows SOPHIE YNS targets, and red shows HARPS Sco-Cen targets. (*a*) Absolute *V*-magnitude vs. *B* − *V*. The solar properties are displayed (yellow stars) for comparison. (*b*) $v \sin i$ vs. *B* − *V* distribution.

(a)

(b)

Fig. 15. Main physical properties of our final combined sample. (*a*) Histogram of the stellar masses (in $M_\odot$). (*b*) Age histogram. The bin size has been chosen to be greater than the standard deviation of the ages of the sample. The HARPS YNS (black) histogram, the SOPHIE YNS (blue) histogram, and the HARPS Sco-Cen (red) histogram are stacked.

BVS and RV[11] (Lagrange et al. 2009). According to these criteria, we report the main origin of the RV variations in Tables A.2, A.4, and A.6.

After removing the signal due to a companion when relevant (cf. Fig. 3), and additionally removing the drift induced by the secular acceleration for HD 217987 (Grandjean et al. 2020), the median of the RV rms of the final combined sample is $54\,\text{m s}^{-1}$ (mean of $153\,\text{m s}^{-1}$) and the ratio of the RV rms and the mean RV uncertainty varies between 1 and 120, with a median at 9. We display in Fig. 19 the mean RV uncertainty versus the *B* − *V*, versus the $v \sin i$, and versus the M_*. We also display the RV rms versus *B* − *V* and versus age in Fig. 20. The mean RV uncertainty is strongly correlated with the $v \sin i$ ($R = 0.84$, $p_{\text{value}} < 4 \times 10^{-47}\%$). This correlation arises because the spectral lines become broader and shallower with increasing $v \sin i$, which decreases our precision on RV computation. In addition, we observe a weak negative correlation between mean RV uncertainty and *B* − *V* ($R = -0.52$, $p_{\text{value}} < 2 \times 10^{-13}\%$). This correlation arises because early-type stars present fewer spectral lines and higher $v \sin i$ than late-type stars, which decreases our precision on the RV computation for these stars.

4.3. RV correction for activity and companions

To obtain the best detection limits, we need to correct the targets RVs for stellar activity and from any known companion signal whenever possible. This has been done in the analyses of the

(a)

Fig. 14. *Gaia* DR2 (Gaia Collaboration 2018) distance histogram of our final combined sample. The HARPS YNS (black) histogram, the SOPHIE YNS (blue) histogram, and the HARPS Sco-Cen (red) histogram are stacked.

4.2. Stellar intrinsic variability

The stars in our final combined sample present strong jitter in their RV time series, which is consistent with the stars being active (solar- to late-type stars) or pulsating (early-type stars). Pulsating stars stars show a vertically spread (BVS, RV) diagram, while stars with magnetic activity present a correlation between

---

[11] This applies when the stellar lines are resolved (Desort et al. 2007), which is the case for our targets (cf. Tables A.1, A.3, and A.5).

(a)

(b)
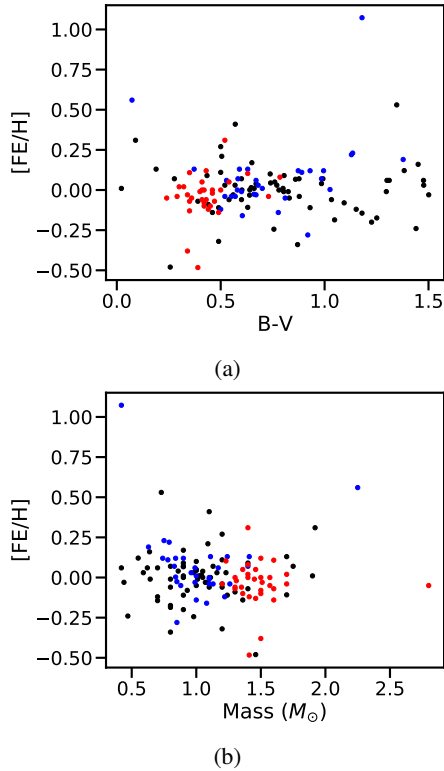
Fig. 16. Metallicity of our final combined sample against $B - V$ (a) and against stellar mass (b). Black shows HARPS YNS targets, blue shows SOPHIE YNS targets, and red shows HARPS Sco-Cen targets.
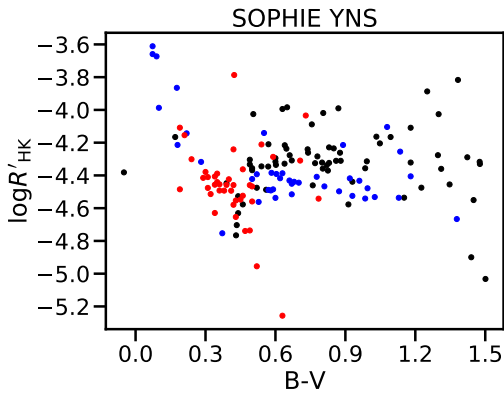
Fig. 17. Final combined sample $\langle \log R'_{\mathrm{HK}} \rangle$ vs. $B - V$. Black shows HARPS YNS targets, blue shows SOPHIE YNS targets, and red shows HARPS Sco-Cen targets.

HARPS and SOPHIE YNS surveys (Grandjean et al. 2020, 2021). Here, we proceeded as in Grandjean et al. (2020):

When the RV variations are mainly due to spots (marked A in the Table A.2), we corrected the RVs for this stellar activity as proposed in Melo et al. (2007): a linear regression between the RVs and the BVS was made and the resulting RV linear function was subtracted from the observed RVs;

When a trend due to a companion was present (cf. Sect. 3.2), we applied a linear regression on their RVs. If the corresponding residuals present a correlation between the BVS and the RVs, we corrected them for this correlation using the Melo et al. (2007) method (cf. point above);

When a companion was present and its properties are well characterized (cf. Sect. 3.2), we used the residuals of the fit. If

these residuals present a correlation between the BVS and the RVs, we corrected them for this correlation again using Melo et al. (2007) method.

The detection limits were then computed using the RV residuals of these corrections.

4.4. Detection limits

We used the local power analysis (LPA; Meunier et al. 2012; Borgniet et al. 2017) to compute the $m_c \sin i$ detection limits for periods between 1 and 1000 days in the GP domain (between 1 and 13 M_{Jup}) and in the BD domain (between 13 and 80 M_{Jup}). The LPA method determines the minimum $m_c \sin i$ for all periods P for which a companion on a circular orbit with a period P would lead to a signal consistent with the data by comparing the maximum power of the periodogram of the synthetic companion to the maximum power of the data periodogram within a small period range around the period P. For a given star, the detection limit is infinite for periods greater than its time baseline. We made this choice because the high jitter and the moderate number of spectra per target prevent us from obtaining a strong constraint on a companion signal that has a period longer than the time baseline.

Then, we computed the completeness function $C(m_c \sin i, P)$ of the final combined sample and of the host star spectral type subsamples described in Sect. 4.1: AF, FK, and M. The completeness for a given pair ($m_c \sin i, P$) corresponds to the fraction of stars in the regarded sample for which a companion with this mass and period is excluded given the detection limits within the sample (Borgniet et al. 2017). To compute the completeness, we excluded the targets for which at least one substellar companion with a period between 1 and 1000 days was discovered during the HARPS Sco-Cen survey, the SOPHIE YNS survey, or the HARPS YNS survey: HD 113337 and HD 149790. We did not take the HJ companion candidate of HD 145467 in this analysis into account because we consider its discovery not robust enough. The 40–90% search completeness of the final combined sample and of the AF, FK, and M subsamples is presented in Fig. 21. We note that 60% of the stars have detection limits below 1 M_{Jup} for periods shorter than 10 days and 40% have detection limits below 5 M_{Jup} for periods shorter than 1000 days (cf. Fig. 21a). Finally, we also computed the search completeness function C_D (Borgniet et al. 2017) of the final combined sample in this period and mass range (cf. Table 1). It is greater than 70% for the AF and FK subsamples of the final combined sample.

4.5. GP and BD occurrence rates

We computed the occurrence rates of GPs (1 to 13 M_{Jup}) and BDs (13 to 80 M_{Jup}) for the whole final combined sample[12] and for different ranges of host star spectral types: AF[13], FK[14], and M[15], and for different ranges of periods: 1–10, 10–100, 100–1000, and 1–1000 days. To do this, we used the method described in Borgniet et al. (2017). For the range without detected companions in the survey, only the upper limits of the occurrence rates can be estimated. The results are presented in Table 1 and in Fig. 22. We find an occurrence rate of $0.7^{+1.6}_{-0.2}\%$ for GPs with periods between 1 and 1000 days and an occurrence rate of $0.6^{+1.4}_{-0.2}\%$ for BDs in the same period range. These values are compatible

---

[12] 176 stars, $B - V \geq -0.05$, $M \in [0.42; 2.8] M_\odot$.

[13] 80 stars, B-$V \in [-0.05 : 0.52[$, $M \sim 1.5 \pm 0.31 M_\odot$.

[14] 87 stars, $B - V \in [0.52 : 1.33[$, $M \sim 0.98 \pm 0.22 M_\odot$.

[15] 9 stars, $B - V \geq 1.33$, $M \sim 0.6 \pm 0.08 M_\odot$.
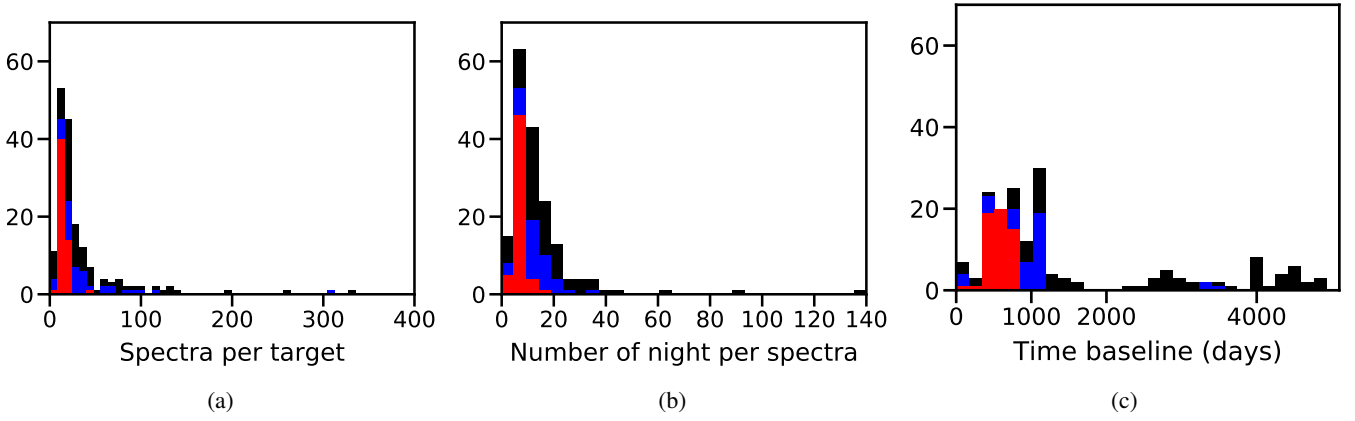
Fig. 18. Observation summary of the final combined sample. (*a*) Histogram of the number of spectra per target, HD 216956 (Fomalhaut, 834 spectra) and HD 039060 (*β* Pic, 5108 spectra) are not displayed. (*b*) Histogram of the number of nights per target. (*c*) Histogram of the time baselines. The HARPS YNS (black) histogram, the SOPHIE YNS (blue) histogram, and the HARPS Sco-Cen (red) histogram are stacked.
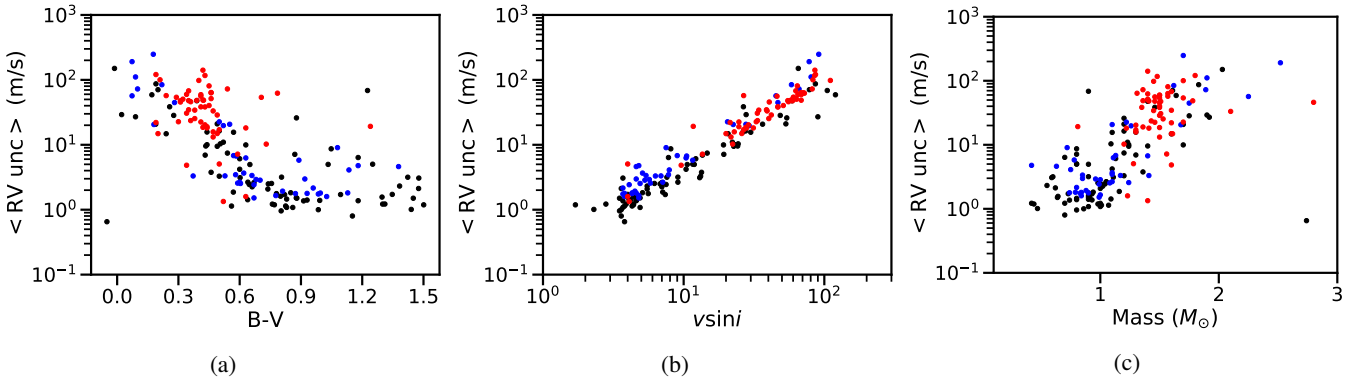
Fig. 19. Summary of the RV uncertainties of the final combined sample. Mean RV uncertainty (accounting for the photon noise only) vs. $B - V$ (*a*), vs. $v \sin i$ (*b*) and vs. $M_\star$ (in $M_\odot$, (*c*)). Black shows HARPS YNS targets, blue shows SOPHIE YNS targets, and red shows HARPS Sco-Cen targets.

(a)

(b)
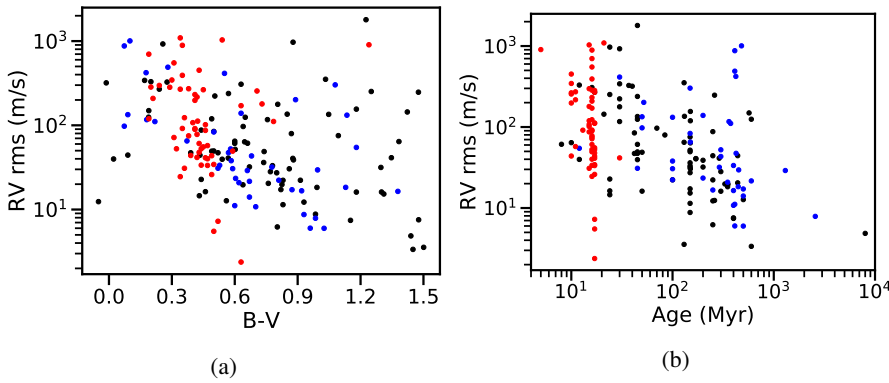
Fig. 20. Summary of the RV rms of the final combined sample. RV rms vs. $B - V$ (*a*), and vs. age (*b*). Black shows HARPS YNS targets, blue shows SOPHIE YNS targets, and red shows HARPS Sco-Cen targets.

within 1σ with those estimated from the HARPS and SOPHIE YNS combined sample (Grandjean et al. 2021). They provide a better estimate, however: the size of the 1σ and 2σ intervals of the occurrence rates is reduced by 25% for GPs. Moreover, through the discovery of HD 149790 B, an occurrence rate for BDs is computed instead of an upper limit.

4.6. Comparison of the occurrence rates for main-sequence stars

In our final combined sample, two systems have substellar companions with periods shorter than 1000 days: HD 113337

(Borgniet et al. 2014, 2019) and HD 149790. Both belong to the AF subsample. However, we may have missed some GPs with low masses and long periods, as only 40% of the stars in our final combined sample have detection limits lower than 5 $M_{\rm Jup}$ between 100 and 1000 days (cf. Fig. 21).

We adopted two statistical tests to compare our results for young stars with those of the surveys carried out on older stars: the $p_{\rm value}$ test, and the pooled version of the two proportion Z-test (which are both described in Appendix D). The null hypothesis that we adopted for these tests is that the occurrence rates of companions in a specific (P, $m_{\rm c} \sin i$) box are identical for the two surveys that are compared. If these tests are passed, then the
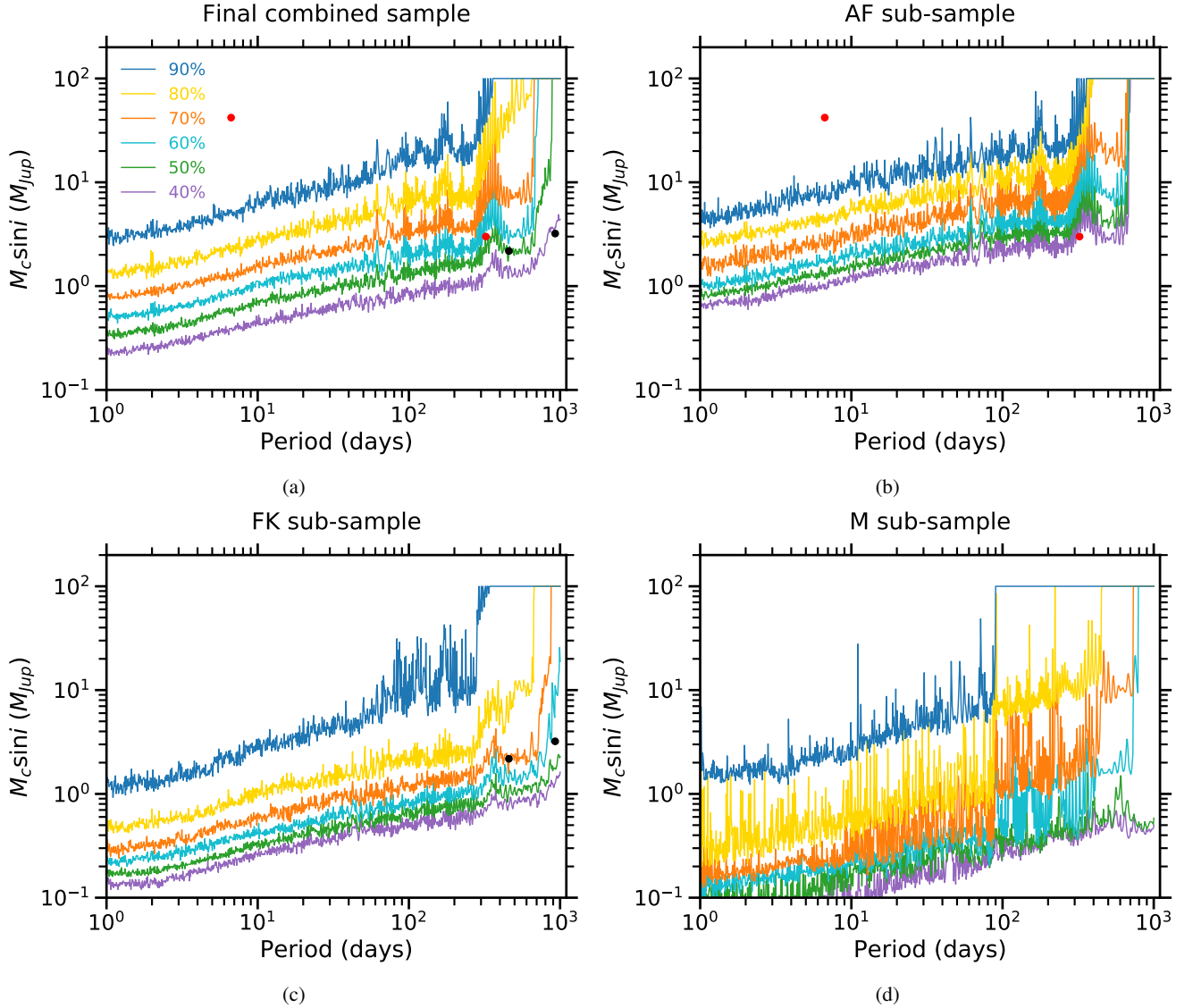
Fig. 21. Search completeness of the whole final combined sample (*a*), and of the AF (*b*), FK (*c*), and M (*d*) subsamples. This corresponds to the lower $m_c \sin i$ for which $X\%$ of the stars in the corresponding sample have detection limits below this $m_c \sin i$ at a given period P; *from bottom to top*: 40% to 90%. Our detected substellar companions HD 113337 b and HD 149790 B are shown as a red dot, while the nondetected planets of the SOPHIE survey, HD 128311 b and c, are shown as black dots (cf. Grandjean et al. 2021).

null hypothesis can be rejected with a confidence level of $1 - \alpha$, indicating a statistical difference between the populations being compared.

4.6.1. Giant planets

In our final combined sample, one GP was detected and confirmed with a period between 1 and 1000 days, HD 113337 b (Borgniet et al. 2014, 2019). In addition, no HJ is firmly detected, and it is unlikely that we missed these objects because 60% of the stars in our final combined sample have detection limits below $1\,M_{\rm Jup}$ between 1 and 10 days, and 80% have detection limits below $3\,M_{\rm Jup}$ in the same period interval.

For A-F stars, an occurrence rate of $1.8^{+4.1}_{-0.5}\%$ for GPs with periods between 1 and 1000 days is found. This is lower than but compatible at 1σ with the occurrence rate of $3.7^{+2.8}_{-1.1}\%$ estimated by Borgniet et al. (2019) around older A-F stars in the same period interval. The *p*-value is $15^{+11}_{-12}\%$, and the Z-test is only validated with a confidence level of 59% (and only the

relaxed criterion of this test, $n > 30$, is validated). We cannot conclude that there is a deficit of GPs with short separations around young A-F stars. Moreover, it should be noted that the survey of Borgniet et al. (2019) has stars in common with the SOPHIE YNS survey; the ages of the two surveys therefore overlap.

For F-K stars, Grandjean et al. (2021) noted a possible lack of young GPs with periods between 1 and 1000 days in comparison to their older counterparts. However, the confidence level of this observation was only 90%. Our Sco-Cen survey only provides a limited number of additional FK-type targets, making it difficult to confirm this observation with a higher level of confidence. In our study, we find an upper limit on the occurrence rate of these planets of $1.3^{+2.9}_{-1.3}\%$, comparable to the $1.4^{+3.1}_{-1.4}\%$ found by Grandjean et al. (2021). This is lower than but still compatible at 1σ with the occurrence rate estimated around older stars of $4.3 \pm 1\%$ (Cumming et al. 2008). The *p*-value is $2^{+3}_{-1}\%$. Thus, there might be a deficit of small-separation GPs around young F-K stars in comparison to their older counterparts, but the

Table 1. GP and BD occurrence rates around young stars.

$m_p \sin i$ interval (M_{Jup})	Orbital period interval (day)	$B - V$	Search completeness C_D (%)	Detected companion Systems	Missed companion systems Upper limit	Companion occurrence rate (%)	Confidence intervals 1σ (%)	2σ (%)
1–13 (GP)	1–10	all	92	0	0.1	<0.6	0–2.0	0–3.5
		[−0.05 : 0.52[	**87**	**0**	**0.2**	**<1.5**	**0–4.8**	**0–8.1**
		[0.52 : 1.33[	*96*	*0*	*0.0*	*<1.2*	*0–3.9*	*0–6.6*
		≥1.33	***99***	***0***	***0.0***	***<11.2***	***0–29.7***	***0–45.6***
1–13	1–100	all	87	0	0.1	<0.7	0–2.1	0–3.7
		[−0.05 : 0.52[	**80**	**0**	**0.2**	**<1.6**	**0–5.2**	**0–8.7**
		[0.52 : 1.33[	*93*	*0*	*0.1*	*<1.2*	*0–4.0*	*0–6.8*
		≥1.33	***97***	***0***	***0.0***	***<11.5***	***0–30.4***	***0–46.6***
1–13	1–1000	all	80	1	0.2	0.7	0.5–2.3	0.2–4.0
		[−0.05 : 0.52[	**71**	**1**	**0.4**	**1.8**	**1.3–5.9**	**0.4–9.9**
		[0.52 : 1.33[	*88*	*0*	*0.1*	*<1.3*	*0–4.2*	*0–7.1*
		≥1.33	***89***	***0***	***0.1***	***<12.5***	***0–33.0***	***0–50.7***
13–80 (BD)	1–10	all	99	1	0.0	0.6	0.4–1.9	0.1–3.2
		[−0.05 : 0.52[	**147**	**1**	**0.0**	**1.3**	**0.9–4.2**	**0.3–7.1**
		[0.52 : 1.33[	*96*	*0*	*0.0*	*<1.2*	*0–3.9*	*0–6.6*
		≥1.33	***100***	***0***	***0.0***	***<11.1***	***0–29.4***	***0–45.2***
13–80	1–100	all	97	1	0.0	0.6	0.4–1.9	0.1–3.3
		[−0.05 : 0.52[	**97**	**1**	**0.0**	**1.3**	**0.9–4.2**	**0.3–7.2**
		[0.52 : 1.33[	*97*	*0*	*0.0*	*<1.2*	*0–3.8*	*0–6.5*
		≥1.33	***100***	***0***	***0.0***	***<11.2***	***0–29.5***	***0–45.3***
13–80	1–1000	all	92	1	0.1	0.6	0.4–2.0	0.1–3.5
		[−0.05 : 0.52[	**91**	**1**	**0.1**	**1.4**	**1.0–4.6**	**0.3–7.7**
		[0.52 : 1.33[	*94*	*0*	*0.1*	*<1.2*	*0–4.0*	*0–6.7*
		≥1.33	***94***	***0***	***0.1***	***<11.8***	***0–31.4***	***0–48.1***

Notes. The parameters are displayed in normal, bold, italic, or bold italic fonts for the full final combined sample, the AF subsample, the FK subsample, or the M subsample, respectively.

confidence level of at least 95% is rather low. A statistical analysis based on a larger number of F-K young targets is needed to determine whether the GPs occurrence rate is significantly lower for young F-K stars than for MS F-K stars.

The occurrence rate of HJs with $m_c \in [1; 13]\, M_{Jup}$ and $P \in [1; 10]$ *days* around F-K stars is found to be lower than $1.2^{+2.7}_{-1.2}\%$, which is similar to the one found for their older counterparts ($1.2 \pm 0.2\%$ Marcy et al. 2005; $0.46^{+0.3}_{-0.3}\%$ Cumming et al. 2008). No massive HJ has been discovered for 87 F-K stars in our final combined sample, the corresponding p-value is $35^{+7}_{-5}\%$ and $67^{+20}_{-15}\%$, respectively. It is possible that the occurrence rate of these planets is identical for young and old stars.

Finally, an occurrence rate of $1.8^{+4.1}_{-0.5}\%$ (against $4.3^{+9.1}_{-1.0}\%$ previously; Grandjean et al. 2021) for A-F stars and an upper limit of the occurrence rate of $1.3^{+2.9}_{-1.3}\%$ (against $1.4^{+3.1}_{-1.4}\%$ previously) for F-K stars is estimated for GPs with periods between 1 and 1000 days. When identical occurrence rates are assumed for young A-F and F-K stars, the p-value of the non-detection of these objects around the 87 stars of our F-K subsample is $21^{+11}_{-21}\%$ (against $25^{+13}_{-24}\%$ previously). There is thus no evidence that the compared populations are different.

4.6.2. Brown dwarfs

A BD with a period between 1 and 1000 days was found in our final combined sample (HD 149790 B), and we

compute an occurrence rate of $0.6^{+1.4}_{-0.2}\%$ for close BDs ($m_c \in [13; 80]\, M_{Jup}$, $P \in [1; 1000]$ *days*). This rate agrees with the results from surveys carried out for older stars, which highlighted that BDs with small separations are rare around the latter (Grether & Lineweaver 2006; Sahlmann et al. 2011; Grieves et al. 2017; Jones et al. 2017; Borgniet et al. 2019; Kiefer et al. 2019).

We find an upper limit on the occurrence rate of close BDs of $1.2^{+2.8}_{-1.2}\%$ for young F-K stars. This agrees with the upper limits on the occurrence rate of these objects derived around older stars of similar spectral types, which was estimated at 1% ($m_c \in [13; 80]\, M_{Jup}$, $P < 5$ yr; Grether & Lineweaver 2006), 0.6% ($m_c \in [13; 80]\, M_{Jup}$, $P < 12$ yr; Sahlmann et al. 2011), 0.56% ($m_c \in [13; 80]\, M_{Jup}$, $P < 300$ days; Grieves et al. 2017), and 2% ($m_c \in [12.5; 90]\, M_{Jup}$, $P < 10\,000$ days; Kiefer et al. 2019). The occurrence rate of close BDs for A-F stars is found to be $1.4^{+3.2}_{-0.4}\%$, which is higher than but still compatible at 1σ with the upper limit found by Borgniet et al. (2019) around older stars of the same spectral types and over the same period interval, $0.5^{+3.1}_{-0.5}\%$. The probability that Borgniet et al. (2019) found no BD on the 225 stars of their sample, knowing the occurrence rate we computed, is $4^{+6}_{-4}\%$. The p-value test is therefore validated with a confidence level of 90%. However, the Z-test is only validated with a confidence level of 52% (and only the relaxed criterion of this test, $n > 30$, is validated). It therefore cannot be concluded that there is an overabundance of close BDs around A-F young stars in comparison to older stars of similar spectral types.
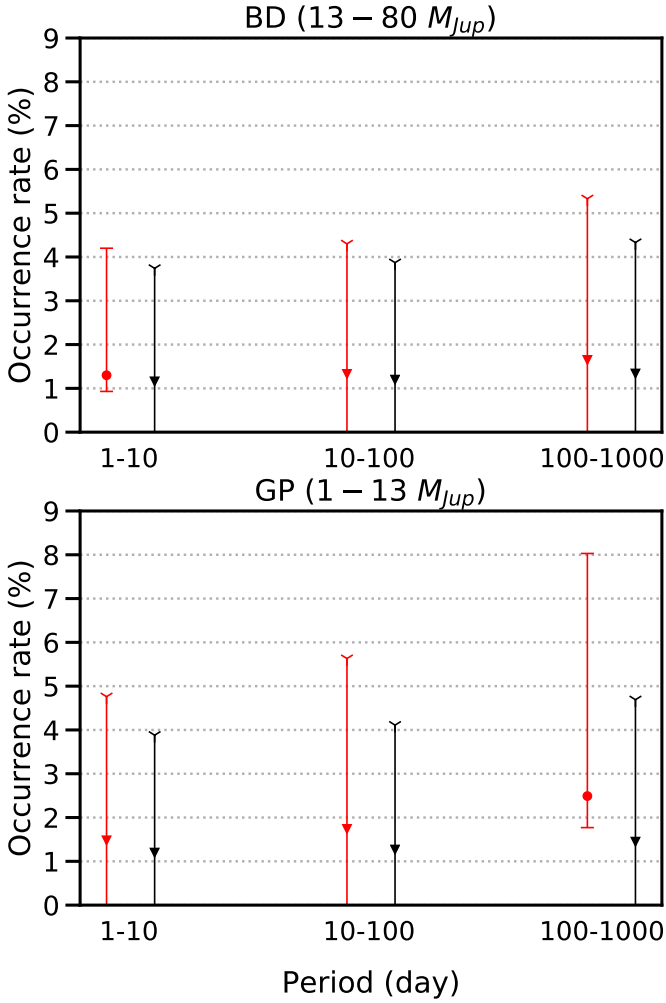
Fig. 22. Occurrence rates (dots) and upper limits on the occurrence rates (triangles) and their respective 1σ ranges for the period ranges of 1–10, 10–100, and 100–1000 days in the GP domain (1–13 M_{Jup}, *top*) and BD domain (13–80 M_{Jup}, *bottom*) for the AF subsample (*red*) and the FK subsample (black).

5. Conclusions

We have carried out a two-year survey of 88 stars of the Sco-Cen association with HARPSin the search for close GPs and BDs companions. Among the stars investigated, one HJ candidate that is yet to be confirmed was found around HD 145467, and one short-period ($P < 10$ days) BD candidate was discovered around HD 149790. In addition, 11 binaries (eight SB1 and three SB2) were identified.

We then combined this survey with the SOPHIE and HARPS YNS surveys presented in Grandjean et al. (2021, 2020), respectively, leading to a statistical analysis of 176 young stars. We obtain an occurrence rate of $0.7^{+1.6}_{-0.2}\%$ for GPs with periods between 1 and 1000 days and a BD occurrence rate of $0.6^{+1.4}_{-0.2}\%$ in the same period range.

We observe a more significant difference in the GP occurrence rates between young and MS FK type stars than was found previously. The associated confidence level is now at 95%, against 90% previously (Grandjean et al. 2021). However, an analysis of a larger number of young stars is still needed to determine whether this difference is really significant.

References

Alsubai, K., Mislis, D., Tsvetanov, Z. I., et al. 2017, AJ, 153, 200
Andrews, J. J., Chanamé, J., & Agüeros, M. A. 2017, MNRAS, 472, 675
Bailey, V., Meshkat, T., Reiter, M., et al. 2014, ApJ, 780, L4
Béjar, V. J. S., Zapatero Osorio, M. R., Pérez-Garrido, A., et al. 2009, in American Institute of Physics Conference Series, 1094, 469
Bohn, A. J., Kenworthy, M. A., Ginski, C., et al. 2019, A&A, 624, A87
Bohn, A. J., Kenworthy, M. A., Ginski, C., et al. 2020a, MNRAS, 492, 431
Bohn, A. J., Kenworthy, M. A., Ginski, C., et al. 2020b, ApJ, 898, L16
Bohn, A. J., Ginski, C., Kenworthy, M. A., et al. 2021, A&A, 648, A73
Bonavita, M., Desidera, S., Thalmann, C., et al. 2016, A&A, 593, A38
Bonavita, M., Gratton, R., Desidera, S., et al. 2022, A&A, 663, A144
Bonnefoy, M., Milli, J., Ménard, F., et al. 2017, A&A, 597, A7
Borgniet, S., Boisse, I., Lagrange, A. M., et al. 2014, A&A, 561, A65
Borgniet, S., Lagrange, A. M., Meunier, N., & Galland, F. 2017, A&A, 599, A57
Borgniet, S., Lagrange, A.-M., Meunier, N., et al. 2019, A&A, 621, A87
Carleo, I., Benatti, S., Lanza, A. F., et al. 2018, A&A, 613, A50
Chauvin, G., Desidera, S., Lagrange, A.-M., et al. 2017a, in SF2A-2017: Proceedings of the Annual meeting of the French Society of Astronomy and Astrophysics, 331
Chauvin, G., Desidera, S., Lagrange, A.-M., et al. 2017b, A&A, 605, A9
Chen, C. H., Mamajek, E. E., Bitner, M. A., et al. 2011, ApJ, 738, 122
Collier Cameron, A., Guenther, E., Smalley, B., et al. 2010, MNRAS, 407, 507
Cotten, T. H., & Song, I. 2016, ApJS, 225, 15
Cox, A. N. 2000, Allen's astrophysical quantities (New York: Springer)
Cumming, A., Butler, R. P., Marcy, G. W., et al. 2008, PASP, 120, 531
da Silva, L., Girardi, L., Pasquini, L., et al. 2006, A&A, 458, 609
Damasso, M., Lanza, A. F., Benatti, S., et al. 2020, A&A, 642, A133
David, T. J., Petigura, E. A., Luger, R., et al. 2019, ApJ, 885, L12
de Zeeuw, P. T., Hoogerwerf, R., de Bruijne, J. H. J., Brown, A. G. A., & Blaauw, A. 1999, AJ, 117, 354
Deleuil, M., Bonomo, A. S., Ferraz-Mello, S., et al. 2012, A&A, 538, A145
Desidera, S., Covino, E., Messina, S., et al. 2015, A&A, 573, A126
Desidera, S., Chauvin, G., Bonavita, M., et al. 2021, A&A, 651, A70
Desort, M., Lagrange, A. M., Galland, F., Udry, S., & Mayor, M. 2007, A&A, 473, 983
Donati, J. F., Bouvier, J., Alencar, S. H., et al. 2020, MNRAS, 491, 5660
Esposito, M., Guenther, E., Hatzes, A. P., & Hartmann, M. 2006, in Tenth Anniversary of 51 Peg-b: Status of and Prospects for Hot Jupiter Studies, eds. L. Arnold, F. Bouchy, & C. Moutou, 127
Figueira, P., Marmier, M., Bonfils, X., et al. 2010, A&A, 513, A8
Gaia Collaboration. 2020, VizieR Online Data Catalog, I/350
Gaia Collaboration (Brown, A. G. A., et al.) 2018, A&A, 616, A1
Galland, F., Lagrange, A. M., Udry, S., et al. 2005a, A&A, 444, L21
Galland, F., Lagrange, A. M., Udry, S., et al. 2005b, A&A, 443, 337
Gallet, F., & Bouvier, J. 2015, A&A, 577, A98
Garufi, A., Benisty, M., Pinilla, P., et al. 2018, A&A, 620, A94
Gáspár, A., Rieke, G. H., & Ballering, N. 2016, ApJ, 826, 171
Grandjean, A., Lagrange, A. M., Keppler, M., et al. 2020, A&A, 633, A44

Grandjean, A., Lagrange, A. M., Meunier, N., et al. 2021, A&A, 650, A39
Grether, D., & Lineweaver, C. H. 2006, ApJ, 640, 1051
Grieves, N., Ge, J., Thomas, N., et al. 2017, MNRAS, 467, 4264
Haffert, S. Y., Bohn, A. J., de Boer, J., et al. 2019, Nat. Astron., 3, 749
Halbwachs, J. L., Kiefer, F., Lebreton, Y., et al. 2020, MNRAS, 496, 1355
Hinkley, S., Kraus, A. L., Ireland, M. J., et al. 2015, ApJ, 806, L9
Huélamo, N., Figueira, P., Bonfils, X., et al. 2008, A&A, 489, L9
Ireland, M. J., Kraus, A., Martinache, F., Law, N., & Hillenbrand, L. A. 2011, ApJ, 726, 113
Jackman, J. A. G., Wheatley, P. J., Bayliss, D., et al. 2019, MNRAS, 489, 5146
Janson, M., Lafrenière, D., Jayawardhana, R., et al. 2013, ApJ, 773, 170
Jones, M. I., Brahm, R., Wittenmyer, R. A., et al. 2017, A&A, 602, A58
Keppler, M., Benisty, M., Müller, A., et al. 2018, A&A, 617, A44
Kervella, P., Arenou, F., Mignard, F., & Thévenin, F. 2019, A&A, 623, A72
Kiefer, F., Halbwachs, J. L., Arenou, F., et al. 2016, MNRAS, 458, 3272
Kiefer, F., Halbwachs, J. L., Lebreton, Y., et al. 2018, MNRAS, 474, 731
Kiefer, F., Hébrard, G., Sahlmann, J., et al. 2019, A&A, 631, A125
Kley, W., & Nelson, R. P. 2012, ARA&A, 50, 211
Lafrenière, D., Jayawardhana, R., & van Kerkwijk, M. H. 2008, ApJ, 689, L153
Lagrange, A. M., Desort, M., Galland, F., Udry, S., & Mayor, M. 2009, A&A, 495, 335
Lagrange, A.-M., Meunier, N., Chauvin, G., et al. 2013, A&A, 559, A83
Lagrange, A.-M., Mathias, P., & Absil, O. 2016, A&A, submitted
Lagrange, A.-M., Keppler, M., Beust, H., et al. 2017, A&A, 608, L9
Lagrange, A. M., Rubini, P., Nowak, M., et al. 2020, A&A, 642, A18
Lang, K. R. 1999, Astrophysical formulae (New York: Springer)
Lieman-Sifry, J., Hughes, A. M., Carpenter, J. M., et al. 2016, ApJ, 828, 25
Mamajek, E. E., Lawson, W. A., & Feigelson, E. D. 1999, ApJ, 516, L77
Mann, A. W., Newton, E. R., Rizzuto, A. C., et al. 2016, AJ, 152, 61
Marcy, G., Butler, R. P., Fischer, D., et al. 2005, Progr. Theor. Phys. Suppl., 158, 24
Mason, B. D., Wycoff, G. L., Hartkopf, W. I., Douglass, G. G., & Worley, C. E. 2001, AJ, 122, 3466
Matthews, E., Hinkley, S., Vigan, A., et al. 2017, ApJ, 843, L12
Matthews, E., Hinkley, S., Vigan, A., et al. 2018, MNRAS, 480, 2757
Mayor, M., Pepe, F., Queloz, D., et al. 2003, The Messenger, 114, 2
McDonald, I., Zijlstra, A. A., & Boyer, M. L. 2012, MNRAS, 427, 343
Melo, C., Santos, N. C., Gieren, W., et al. 2007, A&A, 467, 721
Meunier, N., Lagrange, A. M., & De Bondt, K. 2012, A&A, 545, A87
Mittal, T., Chen, C. H., Jang-Condell, H., et al. 2015, ApJ, 798, 87
Nielsen, E. L., De Rosa, R. J., Macintosh, B., et al. 2019, AJ, 158, 13
Paulson, D. B., & Yelda, S. 2006, PASP, 118, 706
Pecaut, M. J., & Mamajek, E. E. 2016, MNRAS, 461, 794
Pecaut, M. J., Mamajek, E. E., & Bubar, E. J. 2012, ApJ, 746, 154
Pollack, J. B., Hubickyj, O., Bodenheimer, P., et al. 1996, Icarus, 124, 62
Rameau, J., Chauvin, G., Lagrange, A.-M., et al. 2013, ApJ, 772, L15
Rebull, L. M., Stauffer, J. R., Bouvier, J., et al. 2016, AJ, 152, 114
Rizzuto, A. C., Newton, E. R., Mann, A. W., et al. 2020, AJ, 160, 33
Sahlmann, J., Ségransan, D., Queloz, D., et al. 2011, A&A, 525, A95
Ségransan, D., Mayor, M., Udry, S., et al. 2011, A&A, 535, A54
Soto, M. G., Jenkins, J. S., & Jones, M. I. 2015, MNRAS, 451, 3131
Stauffer, J., Rebull, L., Bouvier, J., et al. 2016, AJ, 152, 115
Teyssandier, J., Lai, D., & Vick, M. 2019, MNRAS, 486, 2265
van Eyken, J. C., Ciardi, D. R., von Braun, K., et al. 2012, ApJ, 755, 42
van Leeuwen, F. 2007, A&A, 474, 653
Vigan, A., Fontanive, C., Meyer, M., et al. 2021, A&A, 651, A72
Zucker, S., Mazeh, T., Santos, N. C., Udry, S., & Mayor, M. 2003, A&A, 404, 775
Zucker, S., Mazeh, T., Santos, N. C., Udry, S., & Mayor, M. 2004, A&A, 426, 695

Appendix A: Combined sample

The tables are available at the CDS.

Appendix B: Age and mass estimations

First, the ages and masses of the targets of the HARPS YNS, the SOPHIE YNS, and the HARPS Sco-Cen surveys were taken from the literature when available. We estimated the ages and mass of the remaining ones. Whenever possible, we used the methods described in Desidera et al. (2015) and in Desidera et al. (2021), then in a homogeneous scale with the above works. Briefly, we considered membership to groups and associations (adopting the group ages from Bonavita et al. (2016), also discussed in the upcoming paper), indirect indicators such as rotation, chromospheric and coronal activity, and 6708 Å equivalent width, complemented by isochrone fitting. Preference was given to the moving-group criterion whenever possible (confirmed members). For field objects, the weights assigned to the various methods depend on colors or spectral types and age range (e.g., saturation of chromospheric activity and coronal emission versus age below $100 - 150$ Myr; high sensitivity of lithium to age for K dwarfs younger than $300 - 500$ Myr, with limits only at older ages). Masses were derived using the PARAM interpolation code[16] (da Silva et al. 2006) as in Desidera et al. (2015). For the remaining targets, masses were estimated from an empirical $M_* = f$(B-V) relation. The spectral types were first estimated from the $B - V$ using the relation from Lang (1999) (page 564), and the masses were thereafter deduced from the spectral types by using the relation from Cox (2000) (page 209).

Appendix C: Star with companion data

We present in this appendix the data for the stars with a companion in the HARPS Sco-Cen survey (cf. Fig. 3): RV time series, BVS versus RV diagram, residuals of the companion fit, and bisectors or CCF.

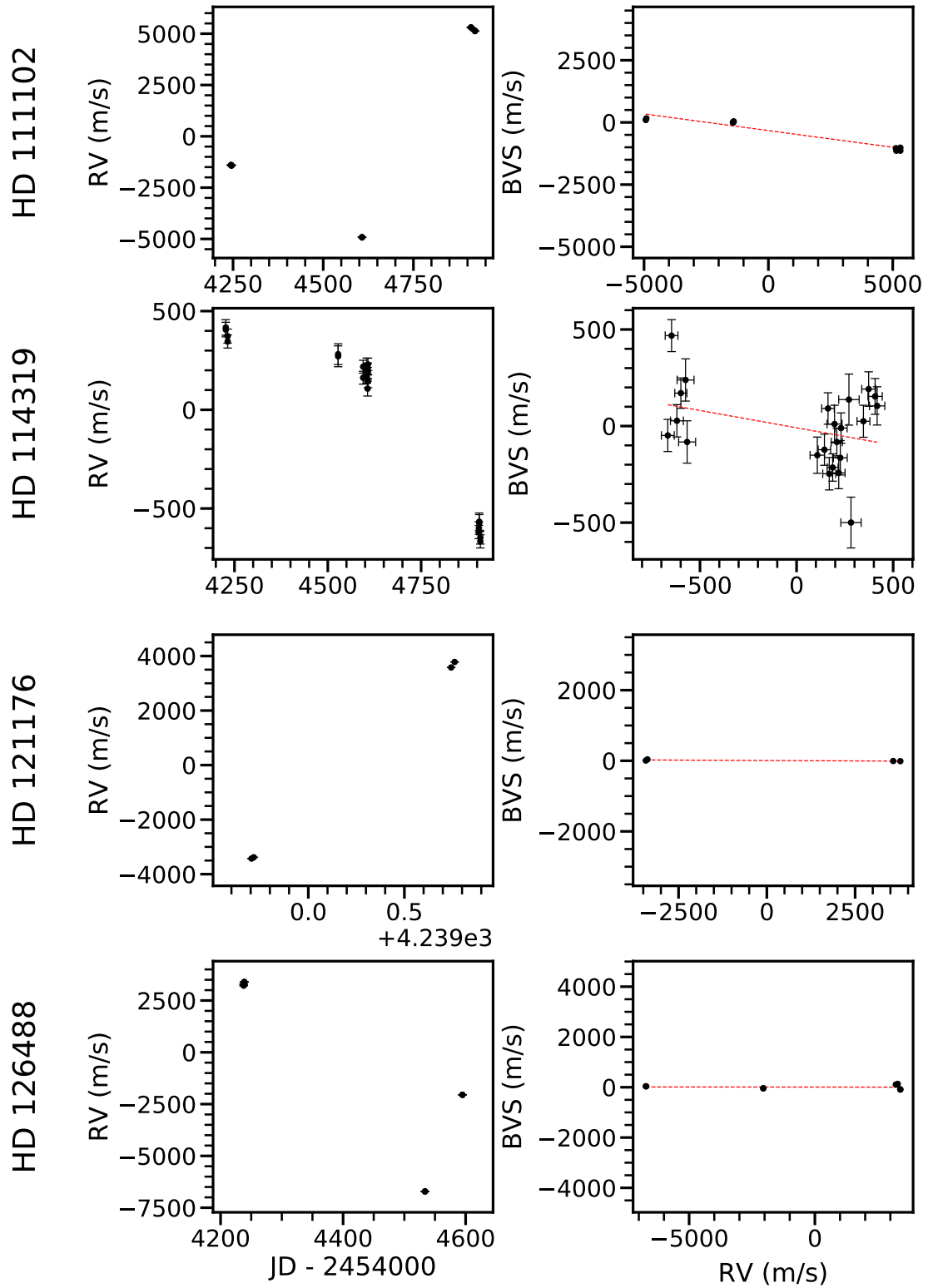[16] http://stev.oapd.inaf.it/cgi-bin/param_1.3

Fig. C.1: Summary of binaries for which orbits could not be derived. *First column*: RV time variations. *Second column*: BVS vs. RV diagram (black) and its best linear model (red dashed line).
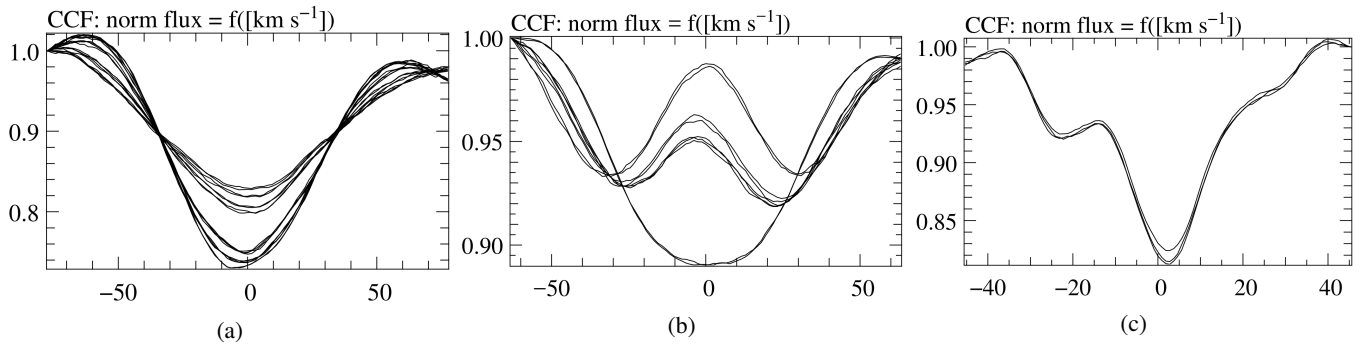
Fig. C.2: CCFs of HD 129590 (a), of HD 137057 (b), and of HD 143811 (c). For these three stars, each curve corresponds to a CCF derived from one of their spectra.
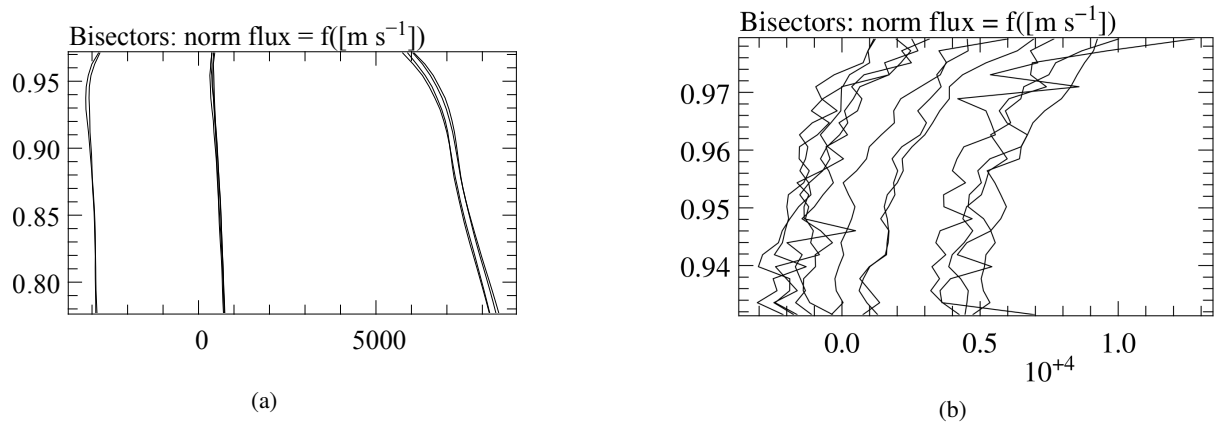

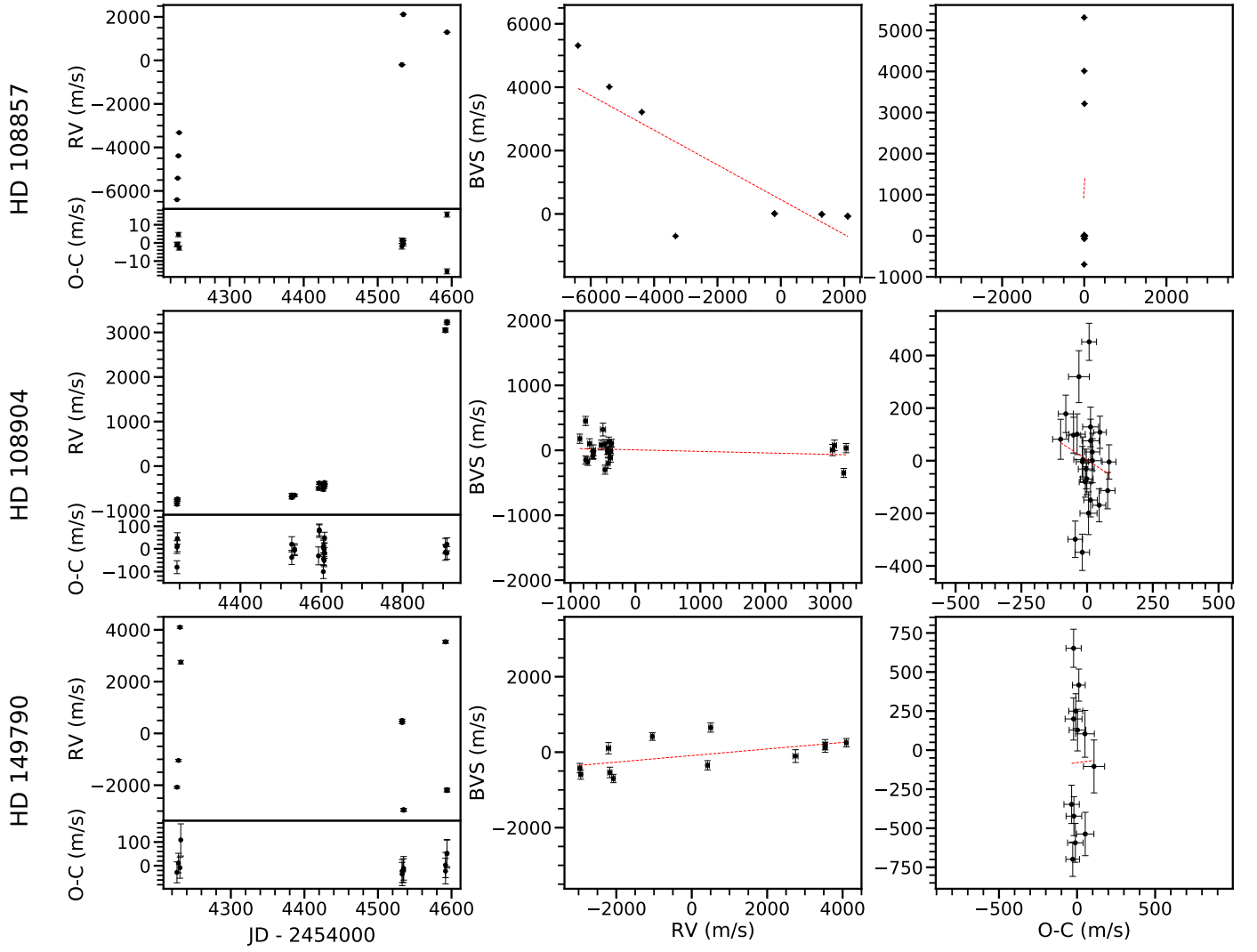Fig. C.3: Bisectors of HD 111102 (a) and HD 149790 (b).

Fig. C.4: RV of the characterized binaries. *First column*: RV time variations (*top*) and Keplerian fit residuals. The fits are presented in Figure 4 for HD 108857, in Figure 5 for HD 108904, and in Figure 9 for HD 149790. *Second column*: BVS vs. RV diagram (black) and its best linear model (dashed red line). *Third column*: BVS vs. RV residuals diagram and its best linear model (dashed red line).

Fig. C.5: Stars with RV trend for which a linear regression was performed. *First column*: *top*: RV time variations (black) with the model of its linear regression (red line). *Bottom*: Residuals of the linear regression. *Second column*: BVS vs. RV diagram (black) and its best linear model (dashed red line). *Third column*: BVS vs. RV residuals diagram and its best linear model (dashed red line).
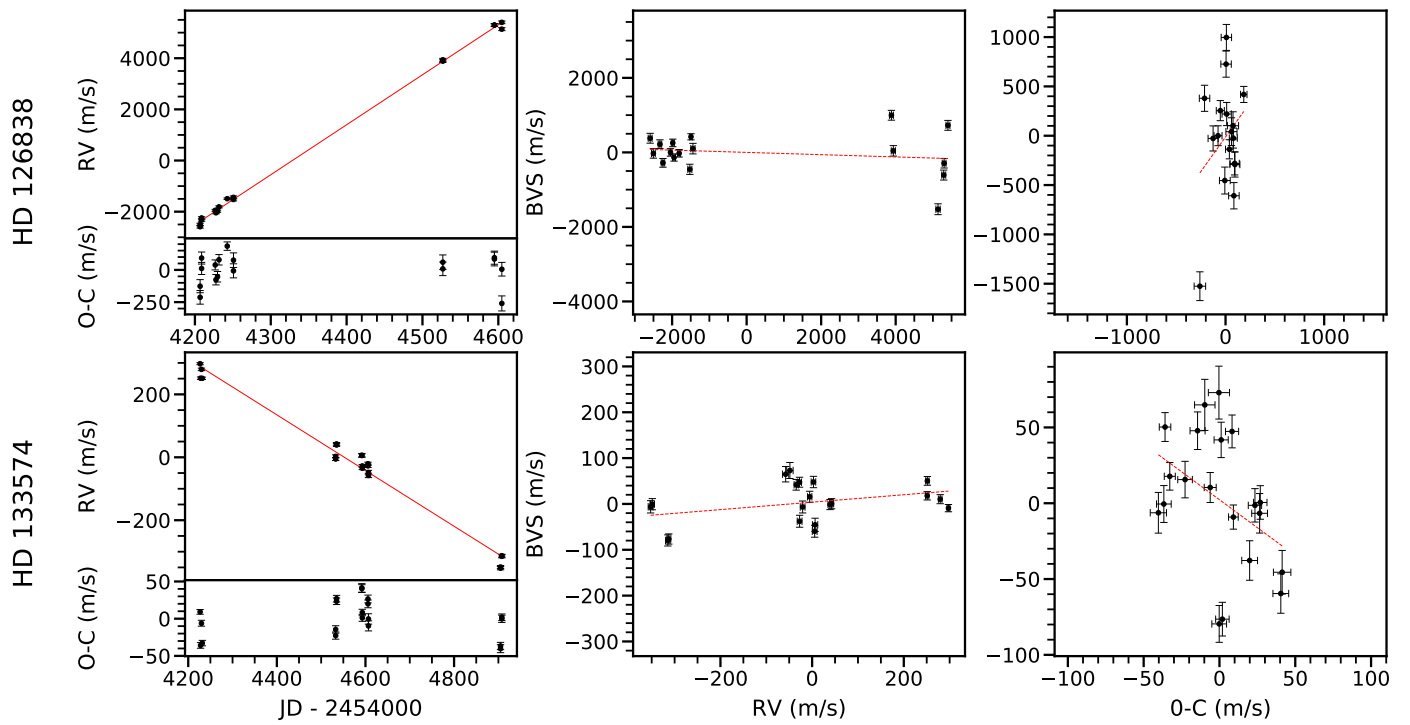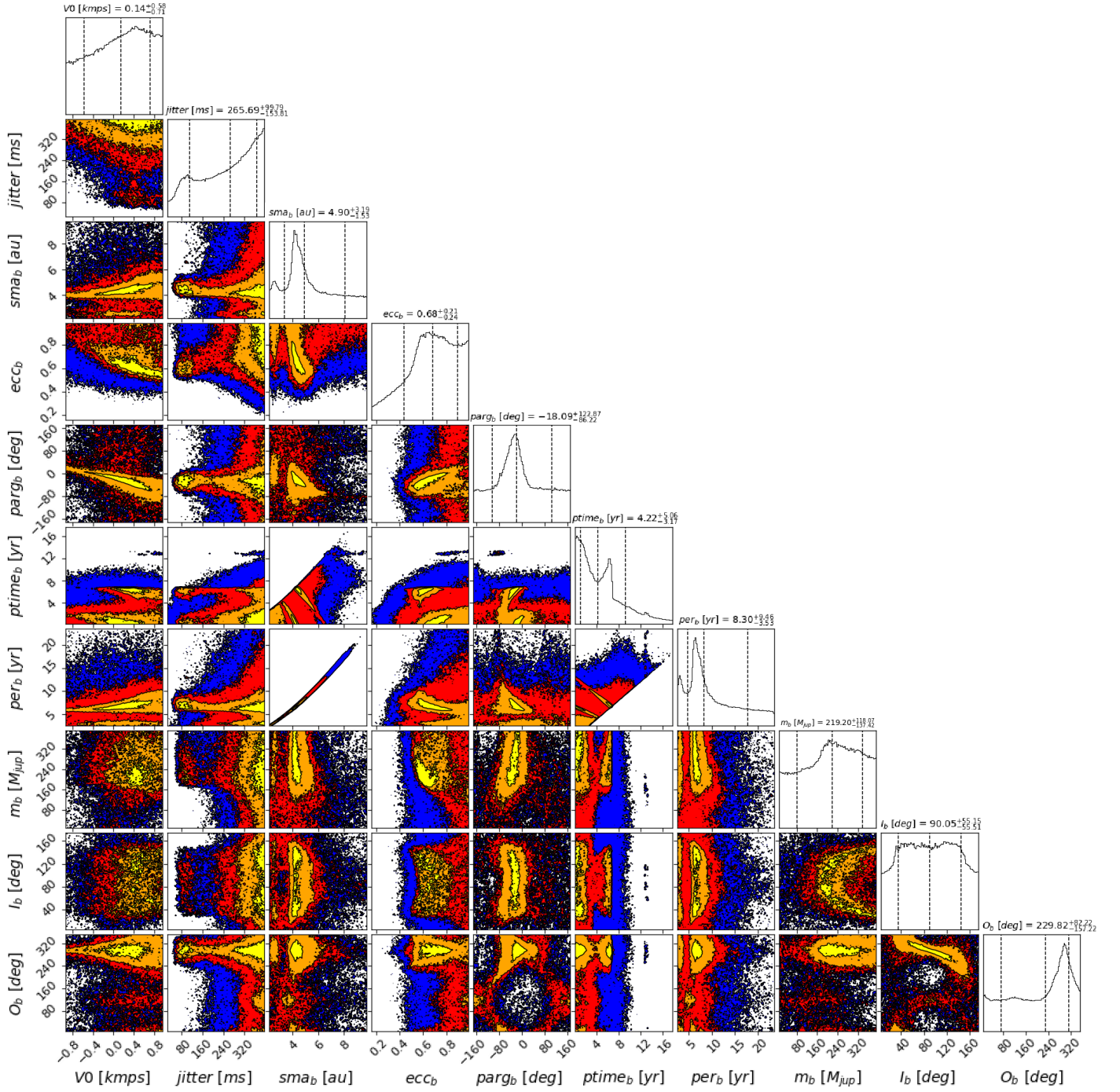
Fig. C.6: Posterior distributions of the MCMC fit performed on the HD 108904 RV and HD 108904 B relative astrometry simultaneously. *From top to bottom:* RV offset to take into account that the RVs are relative to a reference (V_0), RV jitter amplitude (*jitter*), semimajor axis (sma_b), eccentricity (ecc_b), argument of periastron ($parg_b$), period (per_b), mass (m_b), inclination (I_b), and longitude of the ascending node (O_b) of HD 108904 B.

Appendix D: Statistical tests

We present the two statistical tests we used to determine whether the populations of companions studied by different surveys are statistically different (and therefore whether their occurrence rates are statistically different): the p-value test, and the pooled version of the two-proportion Z-test.

These tests are evaluated under a null hypothesis; if a test is validated, then the null hypothesis can be rejected. For these tests, we used the following null hypothesis: the occurrence rate of the two compared companion populations in the studied (P, $M_c \sin i$) box are identical. Thus, if a test is successful and therefore the null hypothesis is rejected, we can deduce that it is unlikely that the occurrence rates of the two compared populations are identical.

For these tests, we assimilated the surveys performed to constrain the companion occurrence rates to Bernoulli tests $\mathcal{B}(n, p)$, with n the number of targets for a given survey and p the actual companion occurrence rate.

Appendix D.1: p-value test

The p_{value} test is a statistical test that evaluates the probability of obtaining the number of observed successes by chance for a given null hypothesis. If this probability is below a validation criterion α, the test is validated.

In our case, we compared two Bernoulli tests ($\mathcal{B}_1(n_1, p_1)$ and $\mathcal{B}_2(n_2, p_2)$) under the following null hypothesis: $p_1 = p_2$. To perform this test, we computed the probability of obtaining the results of the first test (k_1 success among n_1 observations), knowing the probability $p_1 = p_2$:

$$p_{\text{value}} = \binom{n}{k} p_2^{k_1} (1 - p_2)^{n_1 - k_1}$$

with $\binom{n}{k}$ the binomial coefficient of k among n.

If $p_{\text{value}} < \alpha$, the probability of observing the results of the first Bernouilli test under the null hypothesis by chance is below α, and the latter can therefore be rejected with a confidence level of $1 - \alpha$.

Appendix D.2: Pooled version of the two-proportion Z-test

The pooled version of the two-proportion Z-test is a parametric test that allows testing a difference in proportion of successes between two Bernoulli process ($\mathcal{B}_1(n_1, p_1)$ and $\mathcal{B}_2(n_2, p_2)$, respectively).

This test can be used only if the two compared samples are large enough for their probability of success to follow a normal law (as the binomial distribution tends toward a normal distribution when n tends toward infinity). Many criteria are used to ensure it. The most widely used is $n_{1,2} > 30$, but stricter criteria are also used, for example, $n_{1,2} p_{1,2} > 5$; $n_{1,2}(1 - p_{1,2}) > 5$, or $n_{1,2} p_{1,2}(1 - p_{1,2}) > 9$. In our case, only the more relaxed criterion, $n_{1,2} > 30$, is validated.

Then, if these criteria are validated, the difference in the proportion of successes between two Bernoulli process also follows a normal distribution ($\mathcal{N}(\mu, \sigma^2)$). Moreover, in the case of our null hypothesis $p_1 = p_2$, the mean of the normal distribution equals 0. Thus, to test this null hypothesis, we computed the actual difference of the proportion of success between the two compared Bernoulli processes, and we tested whether it actually followed a centered normal distribution ($\mathcal{N}(0, \sigma^2)$). This is the case when

$$\frac{|p_1 - p_2|}{\sqrt{p(1 - p)(\frac{1}{n_1} + \frac{1}{n_2})}} > \mathcal{U}_{1 - \frac{\alpha}{2}}, \tag{D.1}$$

with $p = \frac{n_1 f_1 + n_2 f_2}{n_1 + n_2}$ and with $\mathcal{U}_{1 - \frac{\alpha}{2}}$ the quantile of order $1 - \frac{\alpha}{2}$ of the reduced centered normal distribution.

If Equation (D.1) is verified, the test is validated and the null hypothesis ($p_1 = p_2$) can be rejected with a confidence level of $1 - \alpha$.